The first steps of planet formation : studying grain growth with millimetre interferometers

Lommen, D.J.P.

Chapter 4

Grain growth across protoplanetary discs: 10-μm feature versus mm slope

Abstract

Young stars are formed with dusty discs around them. The dust grains in the disc are originally of the order of 0.1 μm. Models predict that these grains will grow in size through coagulation. Observations of the silicate features around 10 and 20 μm are consistent with a gradual growth from subμm to μm sizes whereas the slope of the spectral energy distribution (SED) at mm and cm wavelengths traces growth up to mm sizes and larger. Grain growth in discs around pre-main-sequence stars is probed in the surface layers of the inner disc by the silicate features and in the mid-plane of the outer disc by the (sub)mm slopes in the SED. We here look for a correlation between these two growth indicators. A large sample of T-Tauri stars was observed with the Spitzer Space Telescope at 5–13 μm and a subsample was observed with the SMA, ATCA, CARMA, and VLA at mm wavelengths. We complement this subsample with data from the literature to maximise the overlap between μm and mm observations and search for correlations in the grain-growth signatures. Synthetic spectra are produced to determine which processes may produce the dust evolution observed in protoplanetary discs. Disc masses in the range $<$ 0.01 to 0.07 $M_\odot$ are obtained. The observations show that the strength and the shape of the 10-μm silicate feature correlate with the slope of the SED between 1 and 3 mm for the sample as a whole. The modelling results confirm that the 10-μm feature becomes flatter and the mm slope shallower with increasing maximum grain size. Assuming a disc with more small grains in the outer disc and more large grains in the inner disc does not enhance the effect. Other processes, such as the flaring angle or the inclination under which the system is observed, usually affect only the mm slope or only the 10-μm feature. The modelling results suggest that, as grains grow, first the 10-μm feature becomes weaker and later the mm slope gets shallower. This quite naturally explains the grouping of sources according to star-forming region in the 10-μm-feature vs mm-slope diagram. Care must be taken when interpreting the size of the grains in the discs from the strength of the 10-μm feature alone.

Dave Lommen, Ewine van Dishoeck, Chris Wright, Sarah Maddison,
David Wilner, Demerese Salter, Michiel Min, Huib Jan van Langevelde,
Geoff Blake, Tyler Bourke, and Remco van der Burg

To be submitted to Astronomy & Astrophysics

4.1 Introduction

The InfraRed Spectrograph (IRS) on-board the Spitzer Space Telescope has provided a wealth of mid-infrared spectra from discs around pre-main-sequence stars (e.g., Kessler-Silacci et al. 2006; Furlan et al. 2006). The spectrum of these objects between 5 and 30 μm is often dominated by silicate emission. Most prominent are the amorphous features at 10 and 20 μm. It was found that the varying strength and the shape of these features can be naturally explained by different grain sizes in the upper layers of the inner disc (Kessler-Silacci et al. 2006), confirming earlier results from the Infrared Space Observatory (e.g., Bouwman et al. 2001) and from the ground (e.g., Przygodda et al. 2003).

Because the 10-μm feature only probes the surface layers of the inner disc, a stronger, more peaked feature could also be due to the settling of larger, micron-sized grains towards the mid-plane. As the larger grains settle and the small ones remain suspended in the upper layers, the surface becomes dominated by small grains, creating a strong silicate band. Dullemond & Dominik (2008) investigated this idea through theoretical models. They find that settling can in principle explain the different shapes of the 10-μm feature, but only in quite specific cases, so that overall grain growth is still the most likely explanation. On the other hand, Voshchinnikov & Henning (2008) find that porosity and the inclusion of crystalline silicates may also have some effect on the shape and strength of the 10-μm feature. Recent interferometric observations of the 10-μm spectral region from $\sim$1 and 2-3-$M_\odot$ objects show that the grains closer to the central star are both larger and more crystalline than those further out in the disc (see, e.g., the recent review by van Boekel 2008). Hence, the evolution of the 10-μm feature may be caused by a combination of grain growth and crystallisation and appears to progress from the inner disc outwards.

Whereas the mid-infrared potentially provides information on the growth of grains from interstellar, submicron sizes to sizes of several microns, the growth to larger sizes can only be probed by submillimetre (submm), millimetre (mm), and occasionally centimetre (cm) observations. Ground-breaking work was done by Beckwith et al. (1990) and Beckwith & Sargent (1991), both analytically studying the emission of dust grains and observing a large sample of young stellar objects at mm wavelengths. More recently, Andrews & Williams (2005) did a sensitive submm continuum single-dish survey of 153 young stellar objects in the Taurus-Auriga star-formation region, including a large amount of archival and literature data. They found that the submm slope between 350 μm and 1.3 mm could be well described by $\alpha = 2.0 \pm 0.5$, where $F_\nu \propto \nu^\alpha$, while the value for the interstellar medium is $\alpha \approx 3.7$ (cf. Draine 2006). Andrews & Williams (2005) inter-

preted this shallow slope as a combined effect of an optically thick contribution and grain growth. It should be noted, however, that the sources in this study were unresolved, and the (sub)mm emission may have a significant contribution from surrounding (envelope) material. More recently, interferometric studies of several dozen T-Tauri stars gave values of $\alpha \lesssim 3.0$ (e.g., Rodmann et al. 2006, and Chapter 3). From this mm slope one can estimate the opacity index $\beta \approx 1.2 \times (\alpha - 2.0)$ (Rodmann et al. 2006) and values of $\beta \approx 1.0$ for $\lambda \gtrsim 1$ mm were found. Such a slope can be naturally explained by a significant fraction of grains at least several mm in size present in the discs (Draine 2006). A subsample of the sources presented in Chapter 3 overlapped with the Spitzer Infrared Spectrograph (IRS) observations published by Kessler-Silacci et al. (2006) and in Chapter 3 we show a tentative correlation between the mm slope of the spectral energy distribution (SED) and the strength and shape of the 10-μm silicate feature for these sources.

Acke et al. (2004) calculated the (sub)mm spectral indices of 26 Herbig-Ae/Be stars, for which the infrared SED could also be determined. They find a correlation between the strength of the ratio of the near- to mid-infrared excess and the slope of the (sub)mm energy distribution for these sources, which they attribute to a correlation between the disc geometry (flared versus self-shadowed) and the size of the grains in the disc. However, the authors do not find a correlation between the strength and the shape of the 10-μm silicate feature and the (sub)mm spectral index (see also Acke & van den Ancker 2004).

In this Chapter, we aim to investigate further the tentative correlation presented in Chapter 3 for a larger sample. A subsample of sources studied with the Spitzer IRS were observed with mm interferometers at longer wavelengths (Section 2). Interferometers were used to ascertain that the emission is dominated by disc emission, as extended emission from surrounding material will be filtered out. Also, spatially resolving the disc ensures that the emission is not optically thick. The results of the observations are shown in Section 3. In Section 4, we present model results for discs that were studied using an advanced radiative-transfer tool. The observations and models are compared and discussed in Section 5. A few conclusions are drawn in Section 6.

4.2 Observations

For this study, we compared Spitzer IRS observations of the 10-μm feature with mm observations from the Very Large Array (VLA, operated by NRAO[1]), the

[1]The National Radio Astronomy Observatory is a facility of the National Science Foundation operated under cooperative agreement by Associated Universities, Inc.

Combined Array for Research in Millimeter-wave Astronomy (CARMA[2]), the Submillimeter Array (SMA[3]), and the Australia Telescope Compact Array (ATCA[4]). A full log of the observations is listed in Sect. 4.7.

4.2.1 Source selection and Spitzer data

To look for possible environmental effects, sources in a total of five star-forming regions were included, spread over the constellations Lupus, Chamealeon, Corona Australis, Serpens, and the Gum nebula at distances of about 150–200, 160, 130, 260, and 400 pc, respectively, see Table 4.1. The sources were pre-selected to have a large spread in the strengths and shapes of the 10-μm features from Spitzer IRS data, mainly the "From Molecular Cores to Planet-forming Discs" programme (c2d, Evans et al. 2003, Program IDs 139 and 172–179) and the "The evolution of dust mineralogy in southern star forming clouds" programme (C.M. Wright PI, Project ID 20611). The spectra from the c2d project were previously published in Kessler-Silacci et al. (2006) and Olofsson et al., (2009, in prep.). Program P20611 includes Spitzer IRS observations from embedded YSOs, T-Tauri stars, and Herbig/Vela-type stars. The results for the T-Tauri stars are presented in this work. All data were re-reduced for this work using the c2d IRS reduction pipeline (Lahuis et al. 2006). Spectra were obtained both integrated over the full aperture of the instrument as well as convolved with the point spread function (PSF) at each wavelength. The Full-Aperture extraction method was used, unless the final spectrum quality of the PSF extraction method was considerably better. Furthermore, only data from the short-low module (SL, 5.2–14.5 μm) data were included, unless data from the short-high module (SH, 9.9–19.6 μm) were present and of significantly higher quality.

In binary systems, it is possible that circumstellar discs get truncated due to binary interaction, affecting grain growth in the discs. To check for such effects, a number of binaries were included in the sample. Furthermore, the sources were selected to include so-called "cold discs" (e.g., Brown et al. 2007). The cold discs

[2]Support for CARMA construction was derived from the Gordon and Betty Moore Foundation, the Kenneth T. and Eileen L. Norris Foundation, the Associates of the California Institute of Technology, the states of California, Maryland, and Illinois, and the National Science Foundation. Ongoing CARMA development and operations are supported by the National Science Foundation under a cooperative agreement, and by the CARMA partner universities.

[3]The Submillimeter Array is a joint project between the Smithsonian Astrophysical Observatory and the Academia Sinica Institute of Astronomy and Astrophysics and is funded by the Smithsonian Institution and the Academia Sinica.

[4]The Australia Telescope Compact Array is part of the Australia Telescope which is funded by the Commonwealth of Australia for operation as a National Facility managed by CSIRO.

Table 4.1: Distances to and ages of star-forming clouds.

Cloud	Age[a] (Myr)	D[b] (pc)
Lupus 1 and 2	$\lesssim 1$	150 ± 20
Lupus 3	1–1.5	200 ± 20
Lupus 4	1–1.5	165 ± 15
Cha I	3–4 (southern subcluster) 5–6 (northern subcluster)	160 ± 15
Corona Australis	5–13	∼130
Serpens	1–15	259 ± 37
Gum nebula	2–6	400 ± 60
Taurus-Auriga	1–10	140 ± 15

[a] Ages adopted from Heiles (1998), Comerón et al. (2003), James et al. (2006), Luhman (2007), Comerón (2008), Kenyon et al. (2008), Neuhäuser & Forbrich (2008), Oliveira et al. (2009), and references therein.

[b] Distances adopted from Brandt et al. (1971), Kenyon et al. (1994), Straižys et al. (1996), Whittet et al. (1997), Bertout et al. (1999), de Zeeuw et al. (1999), Comerón (2008), Neuhäuser & Forbrich (2008), and references therein.

show a lower flux in the mid-infrared, which can be naturally explained by a lack of warm dust close to the star. Several of the cold discs were recently found to be circumbinary discs, with a large hole or gap in the centre, e.g., Espaillat et al. (2007, CS Cha), Guilloteau et al. (2008, HH 30). However, some cold discs are single stars, requiring a different mechanism to clear the inner discs of small, hot grains (e.g., Pontoppidan et al. 2008). One such mechanism could be grain growth into larger particles. A number of cold discs selected from the samples of Brown et al. (2007) and Merín et al. (2008) were included in our source list with the aim to explore this possibility. A full list of the 38 selected sources is given in Tables 4.2 and 4.3. Of these, 28 turn out to have a detected 10-μm feature and 13 yield a mm slope.

4.2.2 SMA observations

A total of 14 sources (including one binary) were observed with the SMA for the project 2007B-S033. The observations were carried out on 14 March and 19 April 2008. The data of 14 March were unusable due to phase instabilities. On 19 April, the phases were stable, and the zenith optical depth at 225 GHz was around $\tau_{225} = 0.13$ all through the night. Physical baselines ranged from 5.8 to 131 metres, resulting in a synthesised beam of about 4.8×2.8 arcsec (natural weighting). The two sidebands were combined into one continuum channel to improve the signal-to-noise ratio, resulting in an effective wavelength of 1.33 mm.

The sources VV CrA (binary), S CrA, and DG CrA were observed as part of the SMA "filler" project 2008A-S111 on 1 October 2008. Only six of the eight antennas were available for this track. However, $\tau_{225} \approx 0.1$ and the phases were stable, resulting in extremely good data. The synthesised beam of the resulting maps was about 5.0×2.1 arcsec (natural weighting). The correlator was tuned to 218 and 228 GHz. Combination of the two sidebands resulted in an effective wavelength of 1.35 mm. The absolute flux calibration of the SMA observations is estimated to be accurate to better than 20%.

4.2.3 ATCA observations

The data for the ATCA project C1794 were taken over the period July to August 2008 when the array was in the H214 configuration. A total of 15 sources were observed: 14 sources (including the binary Sz 65 + Sz 66) were observed at 3 mm and 11 sources at 7 mm. The weather changed considerably over the course of the observations. A short indication of the circumstances for each day is included in Sect. 4.7. Physical baselines ranged from 82 to 247 metres, resulting

in synthesised beam sizes of about 2 arcsec at 3 mm and about 4 arcsec at 7 mm. Combining the two sidebands in the 3 mm band resulted in an effective wavelength of 3.17 mm, those taken in the 7 mm band in an effective wavelength of 6.82 mm. The absolute flux calibration is estimated to be accurate to about 25%.

4.2.4 CARMA observations

A total of 13 sources located in Serpens were observed with the CARMA at 1 and 3 mm in the period April to June 2008 for project c0165. Weather conditions varied over the course of the observations, with a typical water path length of 3–6 mm. The calibrator originally selected for the observations at 1 mm, 1743-038, turned out to be too weak to perform a decent gain calibration, rendering most of the C-configuration observations unusable. For the second part of the observations the telescope was in the D configuration (baselines 11-148 metres), yielding a synthesised beam of about 3×2 arcsec at 1 mm and about 6×4 arcsec at 3 mm. The effective wavelength of the 1 mm-band observations was 1.33 mm, that of the 3 mm-band observations 3.15 mm. The absolute flux calibration is estimated to be accurate to about 30%.

4.2.5 VLA observations

Of the 13 sources in the Serpens star-forming region observed with the CARMA, eight were observed with the VLA at 0.7, 1.3, 3.6, and 6.3 cm under programme AL720. The observations were carried out from 10–15 March, when the array was in the C configuration, with baselines of up to 3.6 km and a synthesised beam of about 0.5 arcsec at 0.7 cm. All observations were performed in the default continuum mode in which, at each frequency, the full 100 MHz bandwidth was used in two adjacent 50 MHz bands. Weather conditions were good in general, with only some clouds forming towards the ends of the tracks carried out on 10 and 13 March. However, a few hours of observing time were lost at the end of the last two tracks due to high winds. The accuracy of the absolute flux calibration is estimated to be about 20% at 0.7 and 1.3 cm and better than 10% at 3.6 and 6.3 cm.

Table 4.2: List of sources in Chamaeleon, Lupus, Corona Australis, and the Gum nebula. The details of the mm observations can be found in Sect. 4.7 and the coordinates of the sources in Sect. 4.8.

Source	Sp. T.	Cloud	Spitzer	Comments
		Vela		
HBC 553	M1.5	Gum	Wright	
HBC 556	M4	Gum	Wright	
HBC 557	K3:	Gum	Wright	
HBC 559		Gum	Wright	
HBC 560	K8	Gum	Wright	
HBC 561	K8	Gum	Wright	Binary[a]
		Chamaeleon		
SZ Cha	K0e	Cha I	GTO	
Sz 32	K4.7	Cha I	c2d	
		Lupus		
IK Lup	K7	Lupus 1	Wright	Binary[b]
Sz 66	M2	Lupus 1	Wright	Binary[b]
HN Lup	M1.5	Lupus 1	Wright	
Sz 77	M0	Lupus 1	Wright	
IM Lup	M0	Lupus 2	c2d	
RY Lup	G0V:	Lupus 3	c2d	
MY Lup		Lupus 4	Wright	
EX Lup	M0	Lupus 3	c2d	
Sz 91	M0.5	Lupus 3	—	Circumbinary[c]
Sz 96	M1.5	Lupus 3	c2d	
Sz 111	M1.5	Lupus 3	—	Cold disc
SSTc2d J161029.57-392214.7		Lupus 3	c2d	Cold disc
SSTc2d J161159.81-382338.5		Lupus 3	c2d	
RX J1615.3-3255	K5	Isolated	c2d	
		Corona Australis		
S CrA	K3	CrA	Wright	Binary[d]
DG CrA		CrA	Wright	
VV CrA	K7	CrA	Wright	Binary[e]

[a] Separation 0.″63 (Correia et al. 2006).

[b] IK Lup (Sz 65) and Sz 66 form a binary with a separation of 6.″4.

[c] Binary star inside IRAC or MIPS point spread functions (Merín et al. 2008).

[d] Separation 1.″3 (e.g., Forbrich et al. 2007, and references therein).

[e] Separation 2.″0.

Table 4.3: List of sources in Serpens. The details of the mm and cm observations can be found in Sect. 4.7 and the coordinates of the sources in Sect. 4.8.

Source	Sp. T.	Cloud	Spitzer	Comments
	Serpens			
SSTc2d J182805.03+000659.3	M4±1	Serpens	c2d	
VV Ser	A2e...	Serpens	c2d	Herbig Ae
SSTc2d J182850.21+000949.7	M5±4	Serpens	c2d	
SSTc2d J182858.09+001724.5	G3±5	Serpens	—	Cold disc
SSTc2d J182900.90+002931.6	K7±2	Serpens	c2d	
CoKu Ser-G3	K0±7	Serpens	c2d	
IRAS 18268-0025		Serpens	c2d	
SSTc2d J182936.20+004216.8	F9±5	Serpens	c2d	
SSTc2d J182944.11+003356.1	M0±1.5	Serpens	c2d	
EC 82	M0	Serpens	c2d	
EC 90	M4±2	Serpens	c2d	Binary[a]
EC 97		Serpens	c2d	
GSC 00446-00153	F3V	Serpens	—	

[a] Separation 1.″5 (e.g., Ciardi et al. 2005, and references therein).

4.3 Results

4.3.1 Mm and cm source fluxes and disc masses

A full log of the results is listed in Sect. 4.8. The results of the interferometric observations at 1, 3, and 7 mm are listed in Tables 4.4 and 4.5.

From the eight sources in Lupus observed with the SMA, four were detected. The four undetected sources had so far also escaped detection in mm surveys, with upper limits quoted for Sz 91 and Sz 96 by Nürnberger et al. (1997) and SSTc2d J161029.6-392215 and SSTc2d J161159.8-382338 being newly detected Spitzer sources. Note, however, that the observations presented here went a factor of two to three deeper those of Nürnberger et al. (1997). Six sources in Lupus were observed with the ATCA at 3.2 mm and all were detected. Five sources were observed at 6.8 mm, of which only one, IM Lup, was detected. MY Lup would have been detected at 6.8 mm with a signal-to-noise ratio of about ten if it had a similar mm slope as IM Lup. However, IM Lup's mm slope between 3.2 and 6.8 mm is rather shallow: $\alpha_{3-7} = 1.82$ (see Table 4.6). Indeed, this is considerably more shallow than the value found for α in Chapter 3 (3.2 ± 0.5), or from interpolating the fluxes at 1.3 and 3.3 mm given in Pinte et al. (2008) ($\alpha_{1-3} = 2.8$).

Three sources in the Gum nebula were observed with the ATCA at 3.2 and at 6.8 mm. None of the sources was detected at either wavelength down to 3σ upper limits of ~3 mJy at 3.2 mm and of ~0.5 mJy at 6.8 mm. This can be attributed to the large distance between us and this star-forming region. If the sources in the Gum nebula had similar fluxes as those in the Lupus clouds, they would have had a flux of ~0.7 mJy, which is below the noise level. Note that, although the Vela molecular ridge has been observed at mm wavelengths (Massi et al. 1999, 2007), no published mm data of the Gum nebula exist in the literature.

The source SZ Cha was detected at 2.3 mJy at 3.2 mm and was not observed at 6.8 mm. Sz 32 was not detected down to a 3σ upper limit of 2.9 mJy at 3.2 mm. It was, however, detected with a flux of 0.77 mJy at 6.8 mm.

VV CrA and S CrA were clearly detected at 1.3 mm with the SMA, with fluxes of 376 and 303 mJy. DG CrA, however, was not detected, down to a 3σ upper limit of only 6.6 mJy. VV CrA and S CrA were also easily detected with the ATCA at 3 and 7 mm. Using uniform weighting to image the binary VV CrA at 3 mm, it was possible to identify the two members. The binary remained unresolved at 1.3 and at 6.8 mm.

Of the 13 sources in the Serpens star-forming region that were observed with the CARMA, only three were detected. This can in part be explained by the

Table 4.4: Fluxes from point-source fits in the (u, v) plane obtained with the SMA and ATCA at 1.3, 3.2, and 6.8 mm and single-dish 1.20-1.27 mm SEST fluxes. 3σ upper limits are quoted in the case of non-detections.

Source	1.3 mm[a]		3.2 mm[b]		6.8 mm		SEST 1.20-1.27 mm[c]	
	Flux (mJy)	rms (mJy/bm)	Flux (mJy)	rms (mJy/bm)	Flux (mJy)	rms (mJy/beam)	Flux (mJy)	rms (mJy)
EX Lup	19	3.9	—	—	—	—	—	—
RY Lup	78	4.9	2.8	0.7	< 0.6[d]	0.21	—	—
Sz 91	< 13[d]	4.3	—	—	—	—	< 27[d]	9
Sz 96	< 13[d]	4.2	—	—	—	—	< 45[d]	15
Sz 111	49	4.8	5.7	0.7	< 0.6[d]	0.19	—	—
SSTc2d J161029.6-392215	< 13[d]	4.4	—	—	—	—	—	—
SSTc2d J161159.8-382338	< 13[d]	4.2	—	—	—	—	—	—
RX J1615.3-3255	132	3.9	6.7	0.6	< 0.5[d]	0.17	—	—
MY Lup	—	—	8.7	0.4	< 0.6[d]	0.20	—	—
Sz 65 & Sz 66	—	—	3.4 & 2.2	0.4	—	—	56 & 47	10 & 12
IM Lup	188	4.3	8.9	1.3	2.2	0.16	260	9
HBC 556	—	—	< 3.7[d]	1.2	< 0.7[d]	0.22	—	—
HBC 557	—	—	< 3.2[d]	1.1	< 0.6[d]	0.18	—	—
HBC 559	—	—	< 2.9[d]	1.0	< 0.3[d]	0.09	—	—
SZ Cha	—	—	2.3	0.4	—	—	77.5	20.3
Sz 32	—	—	< 2.9[d]	1.0	0.77	0.14	93.1	20.8
VV CrA	376	4.5	26.8	1.1	8.3	0.25	469, *584*	21
S CrA	303	3.2	24.9	1.0	3.7	0.20	*290*	—
DG CrA	< 6.6	2.2	< 2.5[d]	0.8	< 0.5[d]	0.16	—	—

[a] 1 mm band observations were at 1.33 mm (Lupus) and at 1.35 mm (Corona Australis).

[b] 3 mm band observations were at 3.17 mm.

[c] SEST fluxes are from Nürnberger et al. (1997, Lupus), Henning et al. (1993, Chamaeleon), and Henning et al. (1994, Corona Australis), with an adopted centre frequency of 236 GHz (1.27 mm). The values in italic are from Chini et al. (2003), with an adopted centre frequency of 250 GHz (1.20 mm).

[d] Quoted value is 3σ upper limit.

Table 4.5: Fluxes from point-source fits in the (u, v) plane obtained with CARMA at 1.3 and 3.2 mm. No sources were detected at 6.8 mm with the VLA; 3σ upper limits are quoted.

Source	1.3 mm[a]		3.2 mm[b]		6.8 mm	
	Flux (mJy)	rms (mJy/bm)	Flux (mJy)	rms (mJy/bm)	Flux (mJy)	rms (mJy/beam)
EC 82	< 15.7[c]	5.2	< 2.9[c]	1.0	< 0.5[c]	0.2
EC 90	95.7	10.4	11.5	1.2	< 1.0[c]	0.3
EC 97	< 23.3[c]	7.8	—	—	< 0.6[c]	0.2
SSTc2d J18290088+0029315	26.4	4.9	3.4	0.5	< 0.7[c]	0.2
IRAS 18268-0025	< 15.6[c]	5.2	< 1.9[c]	0.6	—	—
CoKu Ser-G3	< 17.1[c]	5.7	< 1.8[c]	0.6	< 1.2[c]	0.4
SSTc2d J18285808+0017244	< 24.6[c]	8.2	< 1.9[c]	0.6	—	—
VV Ser	< 14.8[c]	4.9	< 1.8[c]	0.6	< 0.7[c]	0.2
SSTc2d J18285020+0009497	< 22.8[c]	7.6	< 1.9[c]	0.6	< 0.6[c]	0.2
SSTc2d J18294410+0033561	< 15.0[c]	5.0	< 1.7[c]	0.6	—	—
SSTc2d J18293619+0042167	< 8.7[c]	2.9	< 2.9[c]	1.0	—	—
GSC 00446-00153	90.8	3.5	6.8	1.0	—	—
SSTc2d J18280503+0006591	< 8.7[c]	2.9	< 2.9[c]	1.0	—	—

[a] 1 mm band observations were at 1.33 mm.

[b] 3 mm band observations were at 3.15 mm.

[c] Quoted value is 3σ upper limit.

weakness of the other sources, of which six were new Spitzer sources. None of the sources were detected at 6.8 mm using the VLA.

Four cold discs were observed at 1.3 and 3.2 mm for this work. Only one of those, Sz 111, was detected. Unfortunately, Sz 111 was not observed with the Spitzer IRS.

All four binaries that were observed at 1.3 and 3.2 mm were detected at both wavelengths. EC 90 and S CrA remained unresolved. The binary Sz 65+Sz 66 was resolved with the ATCA at 3.2 mm. VV CrA could be resolved with the ATCA at 3.2 mm if the source was imaged using uniform weighting (optimised for resolution). However, this binary remained unresolved with the SMA at 1.3 mm and with the ATCA at 6.8 mm.

The detection rate at mm wavelengths of the sources observed in this study is rather low. This can in part be understood by the distance to the star-forming regions, with the Serpens star-forming region being almost twice as far away as the Taurus-Auriga star-forming region and the Gum nebula in Vela almost three times as far away. This reduces the observed flux for similar sources by a factor of about four to nine. The low detection rate for Lupus is largely a selection effect: most of the brightest sources had been observed before (Chapter 3). These previously detected sources will be included in the analysis below.

Disc masses were obtained from the fluxes at 3.2 mm under the rather crude assumptions of an isothermal disc and a fixed opacity. Under these assumptions, the mass of an optically thin disc is given by $M_{\rm disc} = F_\nu \Psi D^2 / \kappa_\nu B_\nu(T_{\rm dust})$, where Ψ is the gas-to-dust ratio (taken to be 100), D is the distance to the source, κ_ν the dust opacity (taken to be 0.9 cm^2 g^{-1}), and $B_\nu(T_{\rm dust})$ the brightness at the frequency ν for a dust temperature $T_{\rm dust}$, as given by the Planck function. We assumed a dust temperature $T_{\rm dust}$ = 25 K and found disc masses ranging from ~0.004 to ~0.07 $M_\odot$. The disc masses are presented in Table 4.6.

4.3.2 Millimetre slopes

The fluxes at 1, 3, and 7 mm can be combined to obtain the spectral index α, where $F_\nu \propto \nu^\alpha$. We are interested in the emission coming from the dusty disc. However, at 7 mm, other emission mechanisms may contribute significantly to the flux. Sources may include an ionised wind or chromospheric magnetic activity. Rodmann et al. (2006) compare their fluxes at 7 mm to those at 3 and 6 cm and claim that about 20% of the emission at 7 mm is due to free-free emission. On the other hand, in Chapter 5 we show that the emission at 7 mm can be entirely attributed to dust emission for a small sample of three sources. It is possible that the emission due to, e.g., an ionised wind, is quite independent of the disc

mass and thus the relative contribution from such a wind will be larger for young stellar objects that are weaker at mm wavelengths. This could explain the findings presented in Chapter 5, in which some of the strongest pre-main-sequence mm emitters in the southern sky are monitored. However, a larger and more sensitive survey at mm to cm wavelengths is required before more quantitative statements on this subject can be made. Since we do not have fluxes at all three wavelengths for most sources, separate indices will be obtained between 1 and 3 mm (α_{1-3}) and between 3 and 7 mm (α_{3-7}). The results are given in Table 4.6.

The slopes between 1 and 3 mm lie between 2.38 ± 0.36 and 3.83 ± 0.46. Recalling that $\beta \approx 1.2 \times (\alpha - 2.0)$ this corresponds to opacity indices β of about 0.5 to 2.2. The Kolmogorov-Smirnov test gives a probability of 50% that the values from this sample and that of Chapter 3 are drawn from the same distribution. This rather low value is due to the steep slopes for the sources RY Lup (3.83 ± 0.46) and SZ Cha (3.78 ± 0.43). Note that the corresponding values for β are $\gtrsim 2$, whereas the value for the interstellar medium is $\beta_{\rm ISM} \approx 1.7$ (Draine 2006). It is therefore quite likely that other emission mechanisms are contributing at the shorter wavelength and/or that the emission at mm wavelengths is not optically thin for these two sources.

4.3.3 Results from Spitzer infrared observations

The spectra of the T-Tauri stars observed for Spitzer project P20611, including sources in Lupus, Vela, and Corona Australis, are published for the first time here and shown in Fig. 4.1. The 10-μm silicate features were analysed in the ways of both Furlan et al. (2006) and Kessler-Silacci et al. (2006). Furlan et al. (2006) fitted a third-order polynomial to the continuum around the 10-μm feature and determined the integrated flux above and below the continuum. The strength of the 10-μm feature was then defined as the ratio of the integrated flux due to the feature divided by the integrated flux due to the continuum, $(F_{10} - F_{\rm cont})/F_{\rm cont}$, resulting in a strength larger than 0 for a feature in emission. Kessler-Silacci et al. (2006) determined the continuum in three different ways, depending on the full mid-infrared SED and which data were available for each source, and subsequently determined the normalised spectra S_ν according to

$$S_\nu = 1 + \frac{(F_\nu - F_{\nu,c})}{< F_{\nu,c} >}, \tag{4.1}$$

where F_ν is the observed spectrum, $F_{\nu,c}$ is the fitted continuum, and $< F_{\nu,c} >$ is the frequency-averaged continuum flux (see their paper for details). They defined the strength of the 10-μm feature as the maximum value of S_ν between 5 and 13 μm,

Table 4.6: Mm slopes, disc masses, and properties of the 10-μm silicate feature.

Source	α_{1-3}	α_{3-7}	M_{disc}[a] ($M_\odot$)	$\frac{F_{10}-F_{cont}}{F_{cont}}$	$F_{peak}^{10\mu m}$	$\frac{F_{11.3}}{F_{9.8}}$
EX Lup	...	...	...	0.54	2.01	0.73
RY Lup	3.8 ± 0.5	> 2.0	0.005	1.10	3.16	0.66
Sz 96	...	...	...	0.78	2.30	0.82
Sz 111	2.5 ± 0.4	> 2.9	0.011	...	...	...
J161159.8-382338	...	...	...	0.92	2.48	0.84
RX J1615.3-3255	3.4 ± 0.5	> 3.4	0.013	1.25	3.04	0.96
MY Lup	...	> 3.5	0.017	0.54	1.87	0.79
Sz 65	3.0 ± 0.4	...	0.007	0.36	1.51	0.93
Sz 66	3.3 ± 0.4	...	0.004	0.40	1.62	0.92
Sz 74	...	...	...	0.18	1.29	1.03
Sz 77	...	...	...	0.43	1.63	0.94
IM Lup	3.6 ± 0.4	1.8 ± 0.3	0.017	0.52	1.81	0.85
HBC 553	...	...	...	0.22	1.43	0.86
HBC 556	...	...	< 0.051	0.40	1.64	0.99
HBC 557	...	...	< 0.044	0.21	1.37	0.95
HBC 559	...	...	< 0.040	0.39	1.60	0.85
HBC 560	...	...	...	0.29	1.44	1.03
HBC 561	...	...	...	0.43	1.67	0.90
SZ Cha	3.8 ± 0.4	...	0.006	0.71	2.30	0.85
Sz 32	> 3.7	< 1.8	< 0.008	0.14	1.24	1.11
VV CrA	2.5 ± 0.5	2.4 ± 0.5	0.039	...	...	...
S CrA	2.9 ± 0.7	2.5 ± 0.4	0.036	0.34	1.51	0.97
DG CrA	...	...	< 0.004	1.04	2.94	0.67
EC 82	...	...	< 0.017	1.41	3.55	0.67
EC 90	2.5 ± 0.5	...	0.067	0.26	1.40	1.12
EC 97	...	...	...	0.34	1.56	0.90
J18290088+0029315	2.4 ± 0.4	...	0.020	0.15	1.27	0.96
CoKu Ser-G3	...	...	< 0.010	-0.09	0.82	1.17
VV Ser	...	...	< 0.010	0.33	1.45	0.97
J18285020+0009497	...	...	< 0.011	0.36	1.57	0.88
GSC 00446-00153	3.0 ± 0.5	...	0.040	...	...	...

[a] Disc masses estimated from ATCA and CARMA fluxes, assuming a gas-to-dust ratio $\Psi = 100$, a dust opacity $\kappa_\nu = 0.9$ cm^2 g^{-1}, and a dust temperature $T_{dust} = 25$ K.

$S_{peak}^{10\mu m}$, resulting in a value larger than 1 for a feature in emission. Furthermore, Kessler-Silacci et al. (2006) defined the shape of the 10-μm feature as the ratio $S_{11.3}/S_{9.8}$.

For this work, the continuum was consistently chosen for all sources by fitting a third-order polynomial to data between 5.0 and 7.5 μm and between 13.0 and 16.0 μm (cf. Furlan et al. 2006). The regular continuum was used rather than the frequency-averaged continuum, resulting in the peak strength $F_{peak}^{10\mu m}$ and the shape $F_{11.3}/F_{9.8}$. This does not change the results significantly (see Kessler-Silacci et al. 2006).

The results are listed in Table 4.6 and shown in Fig. 4.2. The upper panel of Fig. 4.2 gives $(F_{10} - F_{\rm cont})/F_{\rm cont}$ vs $F_{peak}^{10\mu m}$, showing a clear correlation between the two definitions of the strength of the 10-μm feature. The lower panel gives $F_{peak}^{10\mu m}$ vs $F_{11.3}/F_{9.8}$, also showing a correlation, confirming the results of Kessler-Silacci et al. (2006). It follows that the three methods to quantify the strength or shape of the 10-μm feature give completely consistent results. When comparing the 10-μm feature with the mm slope in Sect. 4.5 below, the strength defined as $(F_{10} - F_{\rm cont})/F_{\rm cont}$ will be used. The source that lies towards the top and to the right of the general trend in the lower panel is RX J1615.3-3255, an isolated source slightly to the north of the Lupus star-forming clouds.

4.3.4 10-μm feature vs mm slope

Figs. 4.3 and 4.4 show the mm slope α, measured between 1 and 3 mm, as a function of the strength of the 10-μm feature $(F_{10} - F_{\rm cont})/F_{\rm cont}$. Included are the sources from this study, as well as those located in the Taurus-Auriga star-forming region discussed in Rodmann et al. (2006) and Andrews & Williams (2007), and those located in Lupus and Chamaeleon and discussed in Chapter 3. In Fig. 4.4, the sources are sorted by their star-forming region.

The mm slope and the strength of the 10-μm feature correlate weakly for the sample shown in Fig. 4.3: the Spearman rank correlation coefficient is 0.50, with a 99.5% confidence level. However, if the point in the lower right (RY Tau) is excluded, the Spearman rank correlation coefficient becomes 0.66, with a 99.99% confidence level.

Fig. 4.4 suggests a grouping in the μm-vs-mm diagram according to parental cloud, with the sources from the Taurus-Auriga star-forming region more concentrated in the lower left, the Lupus sources more to the upper left, and the Chamaeleon sources more to the centre right. Note that the six Lupus sources that are on the left part of the diagram (from top to bottom: IM Lup, Sz 66, Sz 65, RU Lup, GW Lup, and HT Lup) are all located in the Lupus 1 and Lupus 2 clouds,

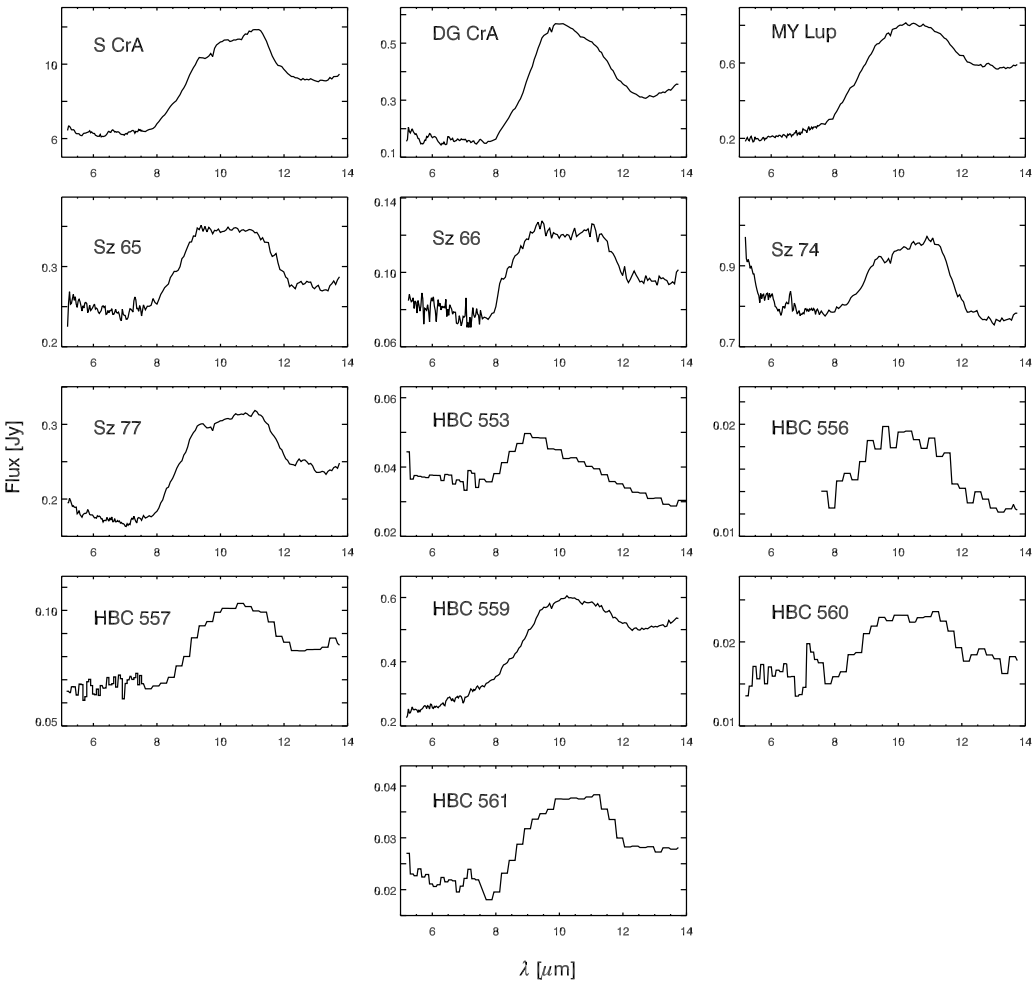

Figure 4.1: Spitzer IRS spectra from the T-Tauri stars observed for Spitzer project P20611 (C.M. Wright PI). Spectra with a maximum flux below 0.1 Jy were binned four times to improve the signal-to-noise ratio.

whereas the remaining two Lupus sources are located in Lupus 3 (top-most source, RY Lup) and off-cloud (RX J1615.3-3255). One explanation for this is that these star-forming regions each represent a different evolutionary phase and/or that each region has a different mechanism dominating the evolution. Another explanation

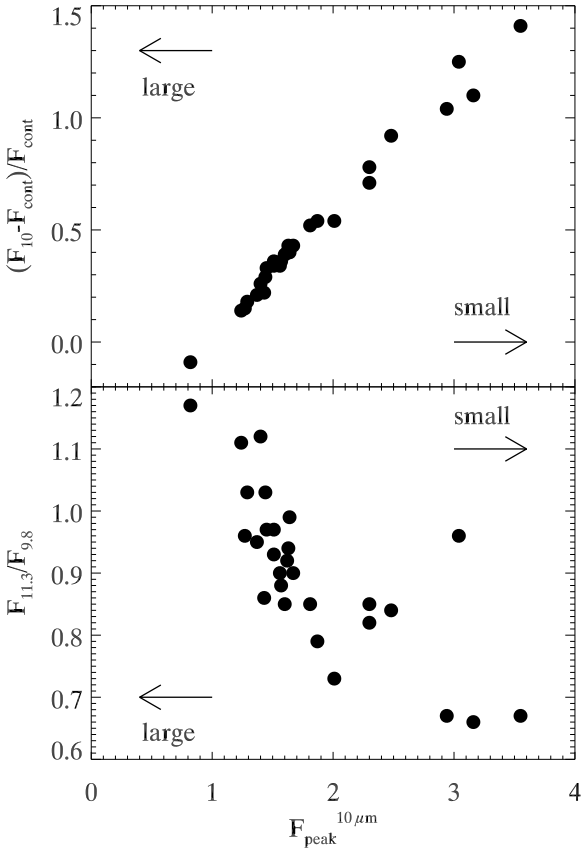

Figure 4.2: *Upper panel*: peak strength of the 10-μm feature as defined in Kessler-Silacci et al. (2006) vs the strength as defined in Furlan et al. (2006). *Lower panel*: peak strength of the 10-μm feature vs the shape as in Kessler-Silacci et al. (2006). Included are the sources observed in this work for which the 10-μm feature could be obtained. The object towards the top and the right off the general trend in the lower panel is the isolated source RX J1615.3-3255.

could be that the different regions have a different mineralogy, e.g., a lower silicate content in the Taurus-Auriga star-forming region than in Chamaeleon, resulting in a weaker 10-μm feature.

Kessler-Silacci et al. (2006) found a correlation between the spectral type of a source and the strength and shape of the 10-μm silicate feature, with brown

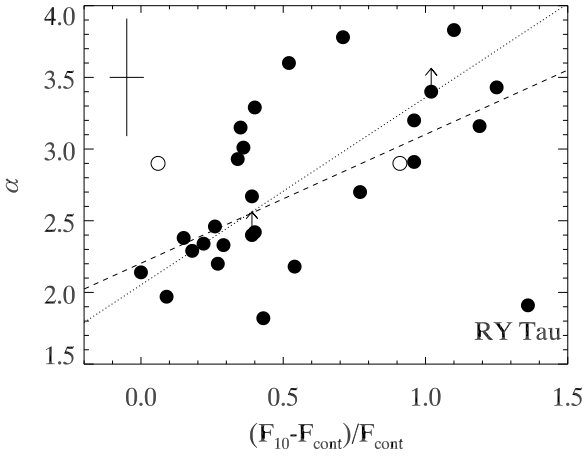

Figure 4.3: The mm slope as measured between 1 and 3 mm as a function of the strength of the 10-μm feature. The open symbol on the left is for T Cha, which does not show any silicate emission and is not used in the analysis; the strength of the 10-μm feature slightly larger than zero is due to PAH emission. The open symbol in the centre is for the circumbinary disc CS Cha. The dashed line shows a linear fit to all the data. The dotted line shows a linear fit to the data with RY Lup (the point in the lower right corner) excluded. Included are the sources studied in this Chapter, as well as those from Rodmann et al. (2006), Andrews & Williams (2007), and Chapter 3. Typical uncertainties are included in the upper left corner.

dwarfs having predominantly flatter and Herbig-Ae/Be stars having more peaked features. It was found that this is most likely due to the location of the silicate emission region (Kessler-Silacci et al. 2007). Kessler-Silacci et al. (2007) found that the radius of the 10-μm silicate emission zone in the disc goes roughly as $(L_*/L_\odot)^{0.56}$. Hence, the 10-μm feature probes a radius further from the star for early-type stars than for late-type stars. In this context it is interesting to see whether a correlation with spectral type is found in the 10-μm-feature vs mm-slope diagram (see Fig. 4.5). The M stars in the sample presented here are concentrated to the left, the F and G stars to the lower left, and the M stars are found more to the centre. Hence, no clear correlation with spectral type is found here. It is interesting to note, though, that the F and G sources RY Tau and RY Lup show up isolated from the other F and G sources. This may indicate that these sources are indeed different from the other sources in the sample, justifying the choice not

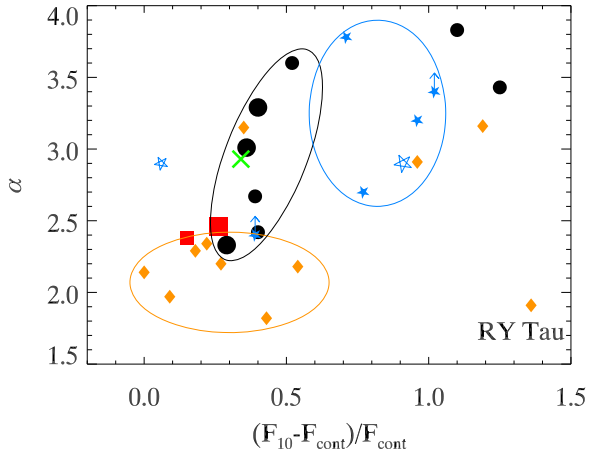

Figure 4.4: Same as Fig. 4.3, with the different sources sorted by star-forming region: *circles*: Lupus, *five-pointed stars*: Chamaeleon, *cross*: Corona Australis, *diamonds*: Taurus-Auriga, and *squares*: Serpens. The ellipses show the concentrations of sources located in the Taurus-Auriga star-forming region (lower left), the Chamaeleon I cloud (top centre), and the Lupus 1 and Lupus 2 clouds (upper left). The remaining two Lupus sources in the upper right are an isolated source (RX J1615-.3-3255, right-most dot) and a source from the Lupus 3 cloud (RY Lup, upper-most dot). The small symbols designate the single stars and the large symbols designate multiple systems. The open five-pointed star to the left is for T Cha, an evolved cold disc which shows no silicate emission around 10 μm. The open five-pointed star in the centre is CS Cha, a circumbinary disc.

to include RY Tau in the analysis.

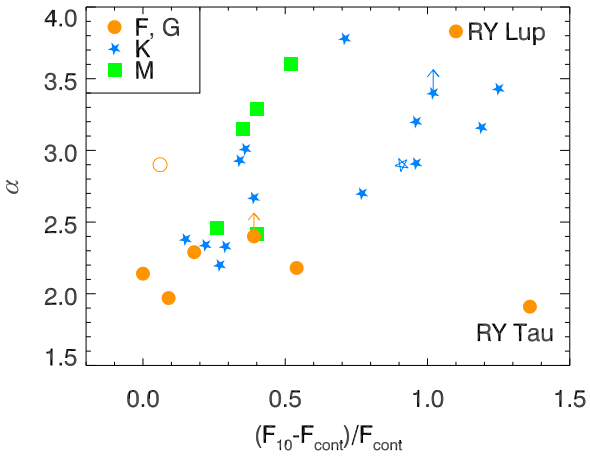

Figure 4.5: Same as Fig. 4.3, with the different sources sorted by spectral type: *circles*: F and G, *five-pointed stars*: K, and *squares*: M.

4.4 Modelling

4.4.1 Disc model parameters and SEDs

As variations in the strength and shape of the 10-μm feature (e.g., Kessler-Silacci et al. 2006) as well as in the (sub)mm slope (e.g., Beckwith et al. 1990) can be explained by variations in the sizes of the grains in the circumstellar discs, one may expect a correlation between properties of the 10-μm feature and the mm slope. We found such a correlation from the observations for the sample as a whole (see previous Section) and this may imply that grain growth occurs in the entire disc simultaneously, or that grains grow in the inner disc and the new grain size distribution is very efficiently spread to the outer disc through radial mixing. Both processes will have the effect of a shift of dust mass from small particles to larger grains. To study this more quantitatively, we ran a number of models with varying grain size distributions.

We use the three-dimensional axisymmetric radiative-transfer code developed by Dullemond (2002) and Dullemond & Dominik (2004a). The disc model is based on the classic model by Chiang & Goldreich (1997), adapted to include a hot inner wall, which is directly irradiated by the central star (Natta et al. 2001, see also Dullemond et al. 2001). The surface density of the disc as a function of radius $\Sigma(r)$ is defined to be:

$$\Sigma(r) = \Sigma_{\rm out}\,(r/R_{\rm out})^n \tag{4.2}$$

with n taken to be $n = -1$. The disc mass was fixed to $M_{\rm disc} = 5 \times 10^{-3}$ M$_\odot$. The gas-to-dust mass ratio Ψ was set to 100, which implies that the total mass in dust grains is also fixed, to a value of 5×10^{-5} M$_\odot$. The variation of the scale height, i.e., the flaring of the disc, was then set by $H(r) = rH_{\rm out}/R_{\rm out}(r/R_{\rm out})^\gamma$. For the radiation field coming from the central star, a black-body spectrum with $T_{\rm eff} = 3000$ K and $L = 1$ L$_\odot$ was used. The inner radius was fixed to $R_{\rm in} = 0.1$ AU, corresponding to a temperature of ~1800 K.

For the dust opacities, we use a mixture of 80% amorphous olivine and 20% armorphous carbon (percentages by mass). The opacities are calculated using a Distribution of Hollow Spheres (DHS, see Min et al. 2003). The total volume of the spheres occupied by the inclusion f is taken in the range $f = [0, 0.8]$. It was found by Dullemond & Dominik (2004a) that the mm slope changes if one goes from a disc with only "small," 0.1-μm-sized particles to a disc that also contains some "large," 2-mm-sized grains. Dullemond & Dominik (2004a) replaced 90%, 99%, 99.9%, 99.99%, and 99.999% of the mass by large grains. However, although the mm slope changes considerably when the mass fraction in large grains

is changed from 0 to 90%, it does not change further if a larger fraction of the dust mass is put in large grains (see Fig. 7 in Dullemond & Dominik 2004a). Although it is possible that a more gradual change in the mm slope is seen when smaller mass fractions are put in large grains, it does seem to be more important what the largest grain size is than which fraction of the dust is contained in such large grains. We therefore chose not to use a bimodal dust distribution, but a distribution in which the size of the grains ranges from a fixed minimum value $a_{\rm min}$ to a varying maximum value $a_{\rm max}$ according to

$$n(a) \propto \left(\frac{a}{a_{\rm min}}\right)^{-m}. \tag{4.3}$$

This power-law distribution is expected on theoretical grounds whenever grain-grain collisions lead to shattering (Dohnanyi 1969). It should be noted that models which include grain growth may lead to different grain size distributions (e.g., Dullemond & Dominik 2005; Tanaka et al. 2005). The value $a_{\rm min}$ was fixed to 0.003 μm and $a_{\rm max}$ was varied in steps of ten from 0.1 μm to 1.0 cm. A value of $m = 3.5$ is representative of interstellar grains (Mathis et al. 1977). A shallower slope of $m = 2.5$ is expected when grains coagulate to larger sizes (Natta et al. 2004, 2007), whereas a slope of $m = 4.0$ is expected when also fragmentation is taken into account (e.g., Dominik & Dullemond 2008). Models run with $m = 4.0$ gave practically no variation of the mm slope, which is an interesting result in itself. It may indicate that the $a_{\rm min}$ is not so small in protoplanetary discs, that the dust size distribution is rather bimodal (or even trimodal) than a power law, or that the grain size distribution is not as steep as models predict. A power-law slope $m = 3.5$ was used for the detailed analysis below. The different model parameters are summarised in Table 4.7.

The resulting SEDs from six models, with $a_{\rm max}$ varying and the other parameters kept fixed, is shown in Fig. 4.6. In these models, $R_{\rm out}$ was fixed to 300 AU, $H_{\rm out}$ to 90 AU, and the flaring angle to $\gamma = 0.14$. Strong variations are seen in all wavelength regimes, from the near-infrared through the mm. At wavelengths $\lambda \lesssim 2$ μm, grain size distributions without grains larger than 1 μm give such a high opacity that the central star is significantly reddened. In the mid- and far infrared, the flux drops with increasing maximum grain size. The (sub)mm part of the SED does not change appreciably unless grains with sizes of $\sim$100 μm or larger are included. After that, the (sub)mm slope becomes shallower quite rapidly with increasing $a_{\rm max}$. This figure also demonstrates that care must be taken when estimating the disc mass from the (sub)mm emission alone: even when the dust species is kept the same, assuming a different grain size distribution may already

Table 4.7: Model parameters.

Parameter	standard value	range
Mass $M_{\rm star}$	1.0 $M_\odot$	
$T_{\rm eff}$	3000 K	
Luminosity $L_{\rm star}$	1.0 $L_\odot$	
Radius $R_{\rm star}$	5.1 $R_\odot$	
Mass $M_{\rm disc}$ ($M_\odot$)	5×10^{-3}	
Disc inclination angle i (°)	45	5.7, 15, 30, 45, 60, 75, 89
Surface mass density gradient n	–1.0	
Gas-to-dust ratio	100	
Inner radius $R_{\rm in}$ (AU)	0.1	
Outer radius $R_{\rm out}$ (AU)	300	100, 200, 300
Disc thickness $H_{\rm out}/R_{\rm out}$	0.3	0.2, 0.3, 0.4
Flaring angle γ	0.14	0.07, 0.14, 0.21

change the opacity at 1 mm by an order of magnitude, which will give an equally large uncertainty in the mass estimate from an observed flux at that wavelength.

4.4.2 10-μm feature vs mm slope

To quantify the evolution of the spectral energy distribution as a function of disc and dust properties, we plot the strength of the 10-μm feature vs the mm slope for different models. The strength of the 10-μm feature $(F_{10} - F_{\rm cont})/F_{\rm cont}$ is defined as in Furlan et al. (2006) and the mm slope α was determined between 1.0 and 3.0 mm. The results are shown in Fig. 4.7. A possible evolutionary path, from small to large grains, is indicated in each panel with arrows.

In the upper left panel, the maximum grain size is varied from $a_{\rm max} = 0.1$ μm to 1, 10, and 100 μm, and finally 1 mm and 1 cm. When $a_{\rm max}$ is changed from 0.1 μm to 10 μm, the strength of the 10-μm silicate feature decreases slightly while the mm slope α is unaffected. When more and more mass is shifted into grains of sizes of 100 μm and larger, the mm slope α becomes shallower, whereas the 10-μm feature is further unaffected.

In the top right panel, the results for models with varying physical disc thickness are shown, with $H_{\rm out}$ = 60, 90, and 120 AU for a fixed outer radius $R_{\rm out}$ = 300 AU. This was done for grain size distributions consisting of only very small grains ($a_{\rm max} = 0.1$ μm), with grains up to 100 μm and for distributions including

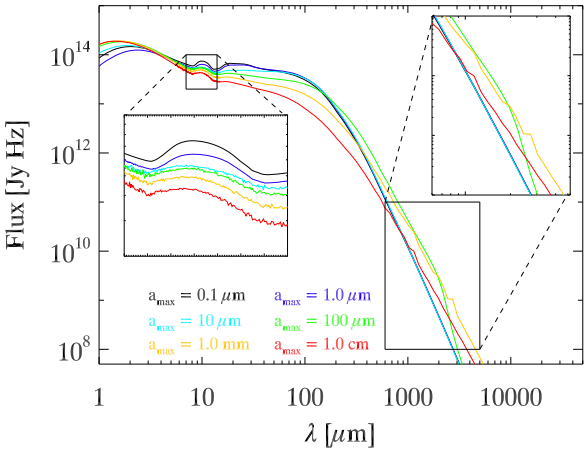

Figure 4.6: Spectral energy distributions (SEDs) for models of a 5×10^{-3} $M_\odot$ disc with a varying grain size distribution, seen under an inclination $i = 45°$. The minimum grain size is 0.003 μm for all models and the maximum grain size varies from 0.1 μm (black curve) to 1.0 cm in steps of ten (lighter curves). The insets show blow-ups from the 10-μm feature and the mm part of the SEDs. Note that the SEDs for $a_{max} = 0.1$ μm, 1.0 μm, and 10 μm are completely overlapping in the mm part.

large grains ($a_{max} = 1$ cm). The thickness of the disc mainly affects the 10-μm feature, largely caused by the fact that the outer disc gets partly in the line of sight between the feature and the observer. In fact, for fairly thick discs with $H/R = 0.4$, the 10-μm feature appears in absorption for grain size distributions with a maximum grain size up to 100 μm (not shown in the plot). The shift in α is mainly due to the difference in a_{max}.

Another way to change the geometry of the disc is by varying the flaring angle γ, as is demonstrated in the middle left panel of Fig. 4.7. R_{out} is fixed to 300 AU, H_{out} to 60 AU, and γ is varied between 0.07, 0.14, and 0.21, for grain size distributions with $a_{max} = 0.1$ μm, $a_{max} = 100$ μm, and $a_{max} = 1$ cm. The mm slope is hardly affected and the effect on the 10-μm silicate feature is again caused by the fact that the outer disc (partly) obscures it from the point of view of the observer. For the smallest grains, the 10-μm feature appears in absorption for $\gamma = 0.21$ (not shown).

The effect of the angle under which the system is observed is demonstrated in

the middle right panel. The inclination is varied from close to face on at 5.7° via 15, 30, and 45° up to a maximum inclination $i = 60°$, for maximum grain sizes $a_{\rm max} = 0.1\,\mu$m, $a_{\rm max} = 100\,\mu$m, and $a_{\rm max} = 1$ cm. In these models, $R_{\rm out} = 300$ AU, $H_{\rm out} = 90$, and $\gamma = 0.14$. No effect on the mm slope α is observed, whereas small variations are seen for the strength of the 10-μm feature. For larger inclinations (for $a_{\rm max} = 0.1\,\mu$m and $a_{\rm max} = 100\,\mu$m already for $i = 60°$, not shown), the 10-μm feature is observed through the outer disc and appears in absorption.

In the lower left panel of Fig. 4.7 the results are shown for discs with outer radii of 300 AU, 200 AU, and 100 AU. The changes in the mm slope α are again mainly due to the change in $a_{\rm max}$, though a trend is observed with the slope becoming steeper as the disc gets larger. The strength of the 10-μm feature is also affected, with the strongest features observed for the largest discs, and the feature actually moving into absorption for a 100-AU disc with $a_{\rm max} = 0.1\,\mu$m.

For each of the models in the lower right panel, four dust size distributions are used. The largest triangle is for a disc with a grain size distribution with $a_{\rm max} = 1$ cm throughout, while the smallest triangle is for a disc with a grain size distribution with $a_{\rm max} = 0.1\,\mu$m throughout. The other triangles represent discs with intermediate stages of grain growth and spreading of large grains, with respectively $a_{\rm max} = 1$ cm, 1 mm, 100 μm, and 10 μm inward of 0.5 AU, $a_{\rm max} =$ 100, 1.0, 0.1, and again 0.1 μm outward of 50 AU, and intermediate grain sizes between 0.5 and 50 AU. A similar effect is seen as in the upper left panel. This seems to suggest that the grain size is the dominating effect for the evolution of the 10-μm feature and the mm slope, rather than the location where the (large) grains reside.

It should be noted that our modelling results do not cover the entire parameter space found from the observations. In particular, the sources with the strongest 10-μm features are not represented by the models. This can at least in part be explained by the fact that settling is not included in the models here. Allowing the largest grains to settle to the mid-plane with the smallest grains suspended in the disc atmosphere will boost the strength of the 10-μm feature. The slope of the grain size distribution m may also have an effect on the strength of the 10-μm feature.

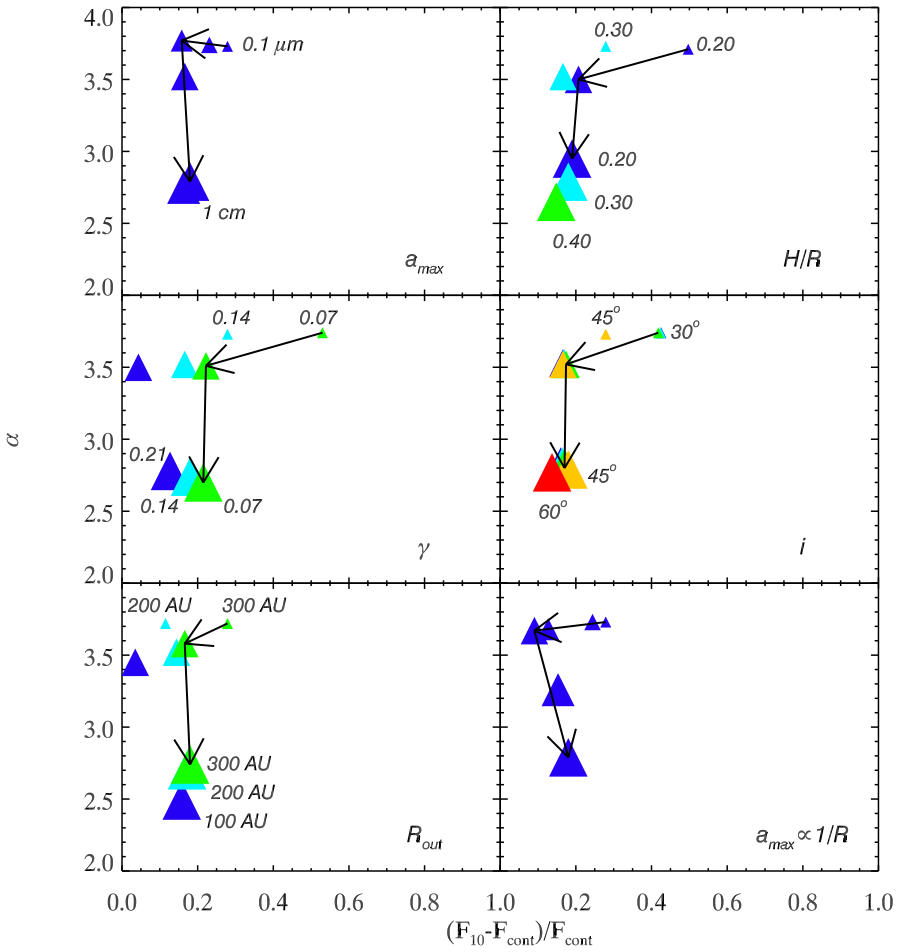

Figure 4.7: The mm slope α vs the strength of the 10-μm feature. See text for disc parameters. The size of the triangles indicates the size of the largest dust grains $a_{\rm max}$; the colour indicates the variation of the other parameters. The arrows indicate an increase in grain size. *Top left*: variation of maximum grain size $a_{\rm max}$ from 0.1 μm to 1, 10, and 100 μm, 1 mm, and 1 cm. *Top right*: variation of disc thickness H/R from 0.20 (dark blue) via 0.30 (light blue) to 0.20 (green). *Middle left*: variation of flaring angle γ from 0.07 (dark blue) via 0.14 (light blue) to 0.21 (green). *Middle right*: variation of inclination i from close to face on (5.7°, dark blue) to 15, 30, 45, and 60° (light blue, green, yellow, and red). *Lower left*: variation of the radius $R_{\rm out}$ from 300 AU (green) via 200 AU (light blue) to 100 AU (dark blue). *Lower right*: variation of maximum grain size with radius.

4.5 Discussion

A correlation between the strength of the 10-μm silicate feature and the slope between 1 and 3 mm is observed in a sample of 27 T-Tauri stars. Put differently, there are no sources with a strong 10-μm feature and a shallow mm slope, nor sources with a weak 10-μm feature and a steep mm slope (with the sole exception of RY Tau). This would suggest that grain growth occurs almost simultaneously throughout the disc or, considering the fact that grain growth will mainly take place in the mid-plane of the inner disc where the densities are highest, that considerable mixing must take place. It also seems to imply that most of the submicron-sized grains are gone by the time the largest grains reach mm sizes. The modelling results do not show such a clear correlation between the strength of the 10-μm feature and the mm slope. It would rather appear that first the 10-μm feature becomes flatter and subsequently the mm slope becomes shallower. Note that this may in part be due to the steep grain size distribution and the very low value for the minimum grain size $a_{\rm min} = 0.003$ μm used in the models.

A gradual over-all change in the grain size distribution as suggested by the observations can also naturally explain the clustering of the sources per star-forming region. The T-Tauri stars in Chamaeleon show the strongest 10-μm features, as well as the steepest mm slopes. The T-Tauri stars located in the Lupus 1 and Lupus 2 clouds have somewhat weaker 10-μm features and mm slopes that are a bit shallower than the Chamaeleon sources. The sources located in the Taurus-Auriga star-forming region, finally, have the weakest 10-μm features and the shallowest mm slopes. This suggests an evolutionary sequence, with the Chamaeleon sources being the least evolved, and the Taurus-Auriga sources the most evolved, although we warn that the samples for each of these clouds are highly incomplete.

Grain size, or rather the maximum grain size, is not the only parameter that affects the observables. It is the dominating effect where the steepness of the mm slope is concerned. However, the strength of the 10-μm feature is also significantly affected by the geometry of the disc and the inclination under which the system is observed. For example, a "self-shadowed" disc, with a small flaring angle γ, gives a much stronger 10-μm feature than a "flaring" disc with a large value for γ. Note that Acke et al. (2004) found a correlation between the single-dish (sub)mm slope between 350 μm and 2.7 mm and the excess at 60 μm for their sample of 26 Herbig-Ae/Be stars, suggesting that grain growth causes a circumstellar disc to evolve from flaring to self-shadowed. However, Acke & van den Ancker (2004) do not find a correlation between the strength of the 10-μm feature and the (sub)mm slope. We also find that a physically flat disc (small value for H/R) gives a strong 10-μm feature, whereas a physically thick disc results in a

weak 10-μm feature. The effect is the strongest for grain size distributions that are strongly dominated by small grains, up to sizes of $\sim$10 μm. One must therefore be very careful when trying to deduce grain sizes, or indeed the physical geometry of the disc, from the strength of the 10-μm feature alone.

It should be noted that our models do not cover the whole range of observed feature strengths and mm slopes. Indeed, 10-μm strengths of $(F_{10} - F_{\rm cont})/F_{\rm cont}$ considerably larger than 1.0 are observed, whereas the values for the models hardly come up to 0.5. This may in part be due to the fact that settling is not taken into account in the models presented here. It is well known that large grains will settle to the disc mid-plane, while the smallest grains remain suspended in the disc atmosphere. We ran a number of models in which we allowed the larger grains to settle and found that the resulting spectra ended up in the upper right of the 10-μm-feature vs mm-slope diagrams. This confirms that the strength of the 10-μm feature is affected by dust settling, as was already found by Dullemond & Dominik (2008) using the same code.

In this context it is interesting to consider another possible relation between the infrared and the mm regimes. The flux around 70 μm, or more generally the mid- to far-IR slope, may be a good tracer of dust settling (e.g., Dullemond & Dominik 2004b). Under the assumption that dust settling is required to get high enough densities for significant grain growth to occur, this would imply a correlation between the slope in the mid-infrared, e.g., between 24 and 70 μm, and the mm slope. As only a small number of the sources for which we obtained reliable mm slopes were observed at several wavelengths with the Multiband Imaging Photometer for SIRTF (MIPS) on board Spitzer, we resorted to IRAS fluxes at 60 and 100 μm to look for this correlation. The results are shown in Fig. 4.8. The top panel shows the IRAS 60-μm fluxes divided by the IRAS 12-μm fluxes vs the mm slope α and the bottom panel shows the IRAS 100-μm fluxes divided by the IRAS 12-μm fluxes vs α. A trend is seen, in particular in the upper panel, for sources with a relatively weak 60-μm flux to have a shallow mm slope. This can be understood as follows. Sources with a weak 60-μm flux are those sources for which the grains of several microns in size have settled to the mid-plane. Thus, in these sources, a large reservoir of micron-sized particles exist in the mid-plane. These particles will collide and grow to mm sizes, in turn causing the mm slope to become shallower.

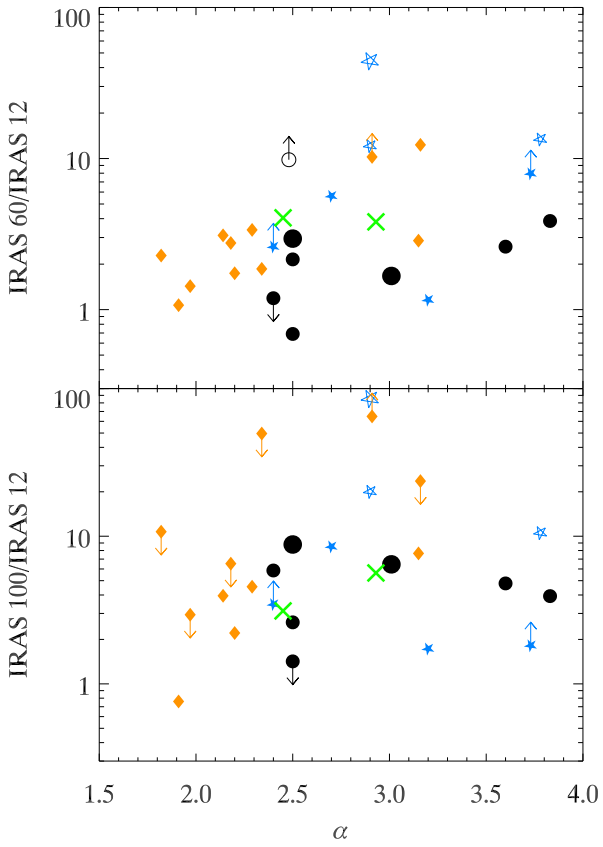

Figure 4.8: *Upper panel*: IRAS flux at 60 μm divided by the flux at 12 μm vs the mm slope α. *Lower panel*: IRAS flux at 100 μm divided by the flux at 12 μm vs the mm slope α. The colour coding of the sources is the same as in Fig. 4.4.

4.6 Conclusions

We observed 38 T-Tauri stars at infrared and mm wavelengths. Combining our new observations with data from the literature, a correlation between the strength of the 10-μm feature and the mm slope was found for the sample as a whole. Modelling protoplanetary discs with varying geometries and grain size distributions indicates that the variations in the 10-μm feature strength and mm slope can be explained by variations in grain size, but that varying disc geometries result in a large spread. While comparing the mm slopes with normalised IRAS fluxes we furthermore found that these show a positive correlation, indicating that the far-infrared slope is already a good tracer of grain growth. This can be understood if one realises that the far infrared traces the amount of settling in a disc and that the sources with the most settling will also be the sources with the most growth and consequently the largest grains.

Acknowledgements
We are indebted to Kees Dullemond for the use of his RADMC and RAYTRACE codes and to Stephen Bourke for help with AIPS. A special thanks to the ATNF and SMA staff for assistance with the observations. Ruud Visser's help on all things computer is greatly appreciated! Partial support for this work was provided by a Netherlands Research School For Astronomy network 2 grant, and by a Netherlands Organisation for Scientific Research Spinoza grant. C.M.W. anknowledges financial support from an ARC Australian Research Fellowship. This research has made use of the SIMBAD database, operated at CDS, Strasbourg, France.

4.7 Appendix: observations

A total of 20 sources (17 in Lupus and three in Corona Australis) were observed at about 1 mm with the Submillimeter Array (SMA). A full log of the SMA observations is given in Table 4.8.

With the Australia Telescope Compact Array (ATCA), 15 sources spread over the constellations Lupus, Vela, Corona Australis, and Chamaeleon were observed at 3 and 7 mm. A log of the ATCA observations is given in Table 4.9.

The Combined Array for Research in Millimeter-wave Astronomy (CARMA) was used to observe ten sources in Serpens at 1 and 3 mm. The log of these observations is presented in Table 4.10.

Finally, eight sources in Serpens were observed with the (Very Large Array) VLA at 0.7, 1.3, 3.6, and 6 cm. A full log of those observations is given in Table 4.11.

Table 4.8: Overview of the SMA observations.

Obs. date	$\lambda\lambda$ (mm)	Config.	Target sources[a]	Gain calibrator(s)	Flux cal.	Notes
20080314[b]	1.30, 1.36	compact	HM Lup, MY Lup, Sz 102, Sz 65 & Sz 66 Sz 73, Sz 74 Sz 76, Sz 77	1517-243, 1626-298	Callisto	PWV < 2.5 mm, bad phases
20080419	1.30, 1.36	compact	EX Lup, RX J1615.3-3255 RY Lup, 161029.6-392215 161159.9-382337, Sz 111 Sz 91, Sz 96	1517-243, 1626-298	Mars	PWV < 4.0 mm
20081001	1.31, 1.37	compact	VV CrA, S CrA, DG CrA	1924-292	Callisto	PWV < 2.5 mm

[a] In the case of SSTc2d names, only the coordinates (in J2000) are shown.

[b] Phase instabilities rendered these observations unusable.

Table 4.9: Overview of the ATCA observations.

Obs. date	$\lambda\lambda$ (mm)	Config.	Target sources	Gain calibrator(s)	Flux cal.	Notes
20080712	3.14, 3.21	H214	HBC 556, HBC 557, HBC 559	0745-330	Mars	Mostly nice weather
20080713	6.67, 6.99	H214	HBC 556, HBC 557, HBC 559	0826-373	Uranus	Weather worsening
20080728	6.67, 6.99	H214	HBC 559	0826-373	Uranus	Mostly nice weather
20080729	3.14, 3.21	H214	HBC 559	0745-330	Uranus	Mostly nice weather
			SZ Cha, Sz 32	1057-797		
20080730	3.14, 3.21	H214	SZ Cha	1057-797	Uranus	Weather less than perfect
20080801	6.67, 6.99	H214	Sz 111, RY Lup	1600-44	Uranus	Weather improving
			RX J1615.3-3255	1622-297		
			VV CrA, S CrA, DG CrA	1921-293		
20080802	3.14, 3.21	H214	SZ Cha	1057-797	Uranus	Weather improving
			Sz 111, RY Lup	1600-44		
			RX J1615.3-3255	1622-297		
			VV CrA, S CrA, DG CrA	1933-400		
20080803	3.14, 3.21	H214	MY Lup	1600-44	Uranus	Mostly nice weather
			VV CrA, S CrA, DG CrA	1933-400		
20080804	3.14, 3.21	H214	Sz 65 & Sz 66	1622-297	Uranus	Weather less than perfect
20080805	6.48, 6.78	H214	MY Lup, IM Lup	1600-44	Uranus	Weather improving

Table 4.10: Overview of the CARMA observations.

Obs. date	$\lambda\lambda$ (mm)	Config.	Target sources[a]	Gain calibrator(s)	Flux cal.	Notes
20080424	1.33	C	EC 82, EC 90, 18290088+0029315	1743-038	3c454.3	Gain cal. too weak
20080426	1.33	C	18290088+0029315, IRAS 18268-0025, CoKu Ser G3, 18285808+0017244, 18285020+0009497, 18294410+0033561, VV Ser	1743-038	3c454.3	Gain cal. too weak
20080501	1.33	C	18293619+0042167, GSC 00446-00153	1743-038	3c454.3	Gain cal. too weak
20080518	1.33	C	GSC 00446-00153	1751+096	3c454.3	
20080521	3.15	C	EC 82, EC 90, 18290088+0029315, IRAS 18268-0025, 18285808+0017244, 18285020+0009497, VV Ser	1743-038	3c273	Gain cal. too weak
20080618	3.15	D	EC 82, EC 90, 18290088+0029315, IRAS 18268-0025, CoKu Ser G3, VV Ser	1751+096	3c279	
20080619	3.15	D	18285808+0017244, 18285020+0009497, 18294410+0033561, 18293619+0042167	1751+096	3c273	
20080620	1.33	D	EC 82, EC 90, 18290088+0029315, IRAS 18268-0025, CoKu Ser G3, VV Ser, 18285808+0017244, 18285020+0009497	1751+096	3c273	
20080622	3.15	D	18293619+0042167, GSC 00446-00153	1751+096	3c273	
20080704	1.33	D	EC 97, 18285020+0009497, 18294410+0033561, 18293619+0042167, GSC 00446-00153	1751+096	3c279	

[a] In the case of SSTc2d names, only the coordinates (in J2000) are shown.

Table 4.11: Overview of the VLA observations.

Obs. date	$\lambda\lambda$ (mm)	Config.	Target sources[a]	Gain calibrator(s)	Flux cal.	Notes
20080310	6.92, 6.93	C	CoKu Ser G3, EC 82 18290088+0029315, EC 90, VV Ser, EC 97, 18285020+0009497	1824+013	3c286	Clouds forming
20080311	13.4	C	CoKu Ser G3, 18290088+0029315, EC 90, VV Ser, EC 97	1851+005	3c286	Clear sky.
20080313	13.4	C	18285020+0009497, 18290980+0034459, EC 82	1851+005	3c286	Clouds forming
20080314	35.5	C	EC 82, EC 90, 18295020+0009497, EC 97, VV Ser,	1804+010	3c286	High winds.
20080315	61.4, 62.0	C	CoKu Ser G3, 18290088+0029315, EC 82, EC 90, 18295020+0009497, EC 97, CoKu Ser G3, 18290088+0029315, VV Ser, 18285020+0009497	1804+010	3c286	High winds.

[a] In the case of SSTc2d names, only the coordinates (in J2000) are shown.

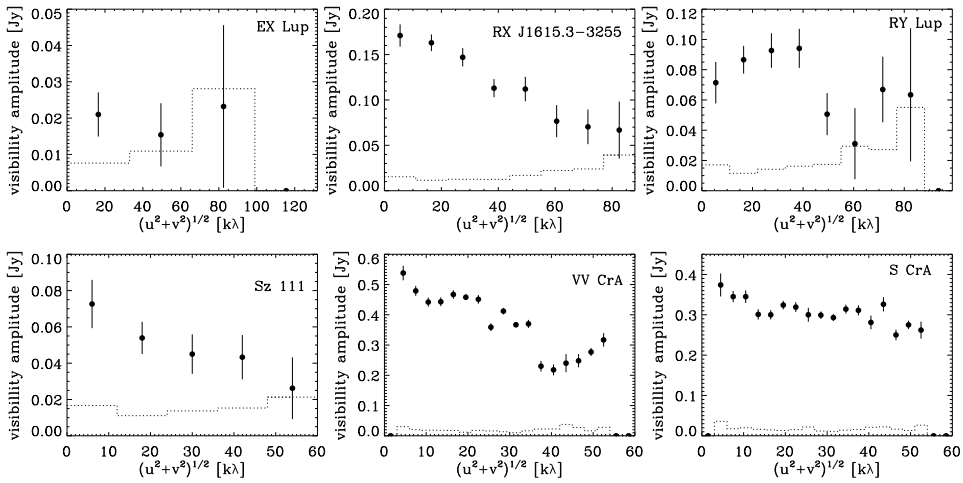

Figure 4.9: Amplitude as a function of (u, v) distance for sources detected with the SMA at 1 mm. The data points give the vector-averaged amplitude per bin, where the data are binned in annuli according to (u, v) distance. The error bars show the statistical 1σ errors and the dotted lines give the expected amplitude for zero signal.

4.8 Appendix: results

The complete results of the SMA observations are shown in Table 4.12. The amplitude as a function of (u, v) distance is plotted in Fig. 4.9.

The complete results of the ATCA observations at 3 mm are shown in Table 4.13, those of the ATCA observations at 7 mm in Table 4.14. Several sources were observed at the same wavelength more than once. The data for those sources were co-added in the (u, v) plane to improve the signal-to-noise ratio. The resulting fluxes or 3σ upper limits are presented in Tables 4.4 and 4.5.

The binary VV CrA was not resolved with the ATCA at 3 or 7 mm using natural weighting, which is optimised for sensitivity. However, using uniform weighting, which is optimised for resolution, the binary could be resolved at 3 mm. The map is shown in Fig. 4.10. The amplitude as a function of (u, v) distance of the sources detected with the ATCA at 3 mm is plotted in Fig. 4.11, that of the sources detected with the ATCA at 7 mm in Fig. 4.12.

The complete results of the CARMA observations at 1 mm are shown in Table 4.15, those of the CARMA observations at 3 mm in Table 4.16. Some sources were observed twice, once in the C and once in the D configuration. If good data

Table 4.12: Complete results of SMA observations at 1.3 mm.

Obs. date	$\lambda_{\rm eff}$ (mm)	Target source[a]	Continuum flux[b] (P)	(G)	rms[c]	Gaussian size (arcsec)	RA[b] (J2000)	Dec[b] (J2000)
20080419	1.34	EX Lup	19.3	21.3	4.0	1.00 ± 1.34	16 03 05.0	-40 18 20.1
		RX J1615.3-3255	131.8	169.1	3.9	1.53 ± 0.13	16 15 20.2	-32 55 05.3
		RY Lup	78.3	89.0	5.0	1.14 ± 0.30	15 59 28.4	-40 21 51.4
		161029.6-392215	< 13.1[d]		4.4	–	16 10 29.6	-39 22 14.4
		161159.9-382337	< 12.7[d]		4.2	–	16 11 59.8	-38 23 38.0
		Sz 111	49.3	52.5	4.2	0.78 ± 0.67	16 08 54.7	-39 37 43.6
		Sz 91	< 13.0[d]		4.3	–	16 07 11.6	-39 03 47.1
		Sz 96	< 12.6[d]		4.2	–	16 08 12.6	-39 08 33.3
20081001	1.35	VV CrA	349.6	367.0	5.1	0.96 ± 0.06	19 03 06.8	-37 12 49.3
		S CrA	301.4	322.2	3.5	0.91 ± 0.07	19 01 08.6	-36 57 20.6
		DG CrA	< 6.6[d]		2.2	–	19 01 55.2	-37 23 40.5

[a] In the case of SSTc2d names, only the coordinates (in J2000) are shown.

[b] Continuum flux and position are from fits in the (u, v) plane. For sources that were detected at 3σ, both the point-source flux (P) and the integrated flux for a Gaussian (G) are shown. For sources that were not detected, the coordinates of the phase centre are quoted.

[c] Calculated from the cleaned image.

[d] Quoted value is 3σ upper limit.

Table 4.13: Complete results of ATCA observations at 3 mm.

Obs. date	$\lambda_{\rm eff}$ (mm)	Target source	Continuum flux[a] (P)	(G)	rms[b]	Gaussian size (arcsec)	RA[a] (J2000)	Dec[a] (J2000)
20080712	3.18	HBC 556		< 3.7	1.2	–	8 10 31.3	-36 01 46.5
		HBC 557		< 3.2	1.1	–	8 12 47.4	-36 19 18.0
		HBC 559		< 3.3	1.1	–	8 13 56.4	-36 08 02.1
20080729	3.18	HBC 559		< 4.3	1.4	–	8 13 51.0	-36 08 02.1
		SZ Cha		< 3.0	1.0	–	10 58 10.0	-77 17 17.6
		Sz 32		< 2.9	1.0	–	11 09 48.0	-76 34 26.0
20080730	3.18	SZ Cha	3.4	5.8	0.5	1.95 ± 0.63	10 58 16.6	-77 17 17.0
20080802	3.18	SZ Cha		< 2.9	1.0	–	10 58 15.5	-77 17 17.6
		Sz 111	5.7	–[d]	0.7	–	16 08 54.6	-39 37 53.3
		RY Lup		< 2.3	0.8	–	15 59 28.0	-40 21 51.2
		RX J1615.3-3255	6.8	–[c]	0.6	–	16 15 20.2	-32 55 05.6
		VV CrA a	31.0	69.5[d]	1.2	2.56 ± 0.21[d]	19 03 06.8	-37 12 49.8
		VV CrA b	25.1	69.5[d]		2.56 ± 0.21[d]	19 03 06.9	-37 12 48.3
		S CrA	22.0	–[c]	1.1	–	19 01 08.6	-36 57 20.2
		GN 18.57.8	7.1	13.1		1.45 ± 0.52	19 01 07.9	-36 57 16.9
		DG CrA		< 3.0	1.0	–	19 01 54.9	-37 23 40.5
20080803	3.18	MY Lup	8.7	–[c]	0.4	–	16 00 44.5	-41 55 31.2
		VV CrA a	23.0	44.2[d]	1.9	2.28 ± 0.38[d]	19 03 06.8	-37 12 49.9
		VV CrA b	21.9	44.2[d]		2.28 ± 0.38[d]	19 03 06.9	-37 12 48.4
		S CrA	24.9	–[c]	1.9	–	19 01 08.6	-36 57 20.6
		GN 18.57.8	8.2	–[c]		–	19 01 07.9	-36 57 15.2
		DG CrA		< 4.3	1.4	–	19 01 54.9	-37 23 40.5
20080804	3.18	Sz 65	3.4	–[c]	0.4	–	15 39 27.7	-34 46 17.6
		Sz 66	2.2	–[c]		–	15 39 28.2	-34 46 17.9

[a] Continuum flux and position are from fits in the (u, v) plane. For sources that were detected at 3σ, both the point-source flux (P) and the integrated flux for a Gaussian (G) are shown. For sources that were not detected, the coordinates of the phase centre are quoted and 3σ upper limits are quoted.

[b] Calculated from the cleaned image.

[c] No circular Gaussian could be fit to the source in the (u, v) plane.

[d] Value is for the two components of VV CrA combined.

Table 4.14: Complete results of ATCA observations at 7 mm.

Obs. date	$\lambda_{\rm eff}$ (mm)	Target source	Continuum flux[a] (P)	(G)	rms[b]	Gaussian size (arcsec)	RA[a] (J2000)	Dec[a] (J2000)
20080713	6.83	HBC 556		< 0.7[c]	0.2	–	8 10 31.6	-36 01 46.5
		HBC 557		< 0.4[c]	0.1	–	8 12 47.7	-36 19 18.0
		HBC 559		< 0.6[c]	0.2	–	8 13 56.8	-36 08 02.1
20080728	6.85	HBC 559		< 0.3[c]	0.1	–	8 13 56.8	-36 08 02.1
20080801	6.85	Sz 111		< 0.6[c]	0.2	–	16 08 53.8	-39 37 43.1
		RY Lup		< 0.6[c]	0.2	–	15 59 27.5	-40 21 51.2
		RX J1615.3-3255		< 0.5[c]	0.2	–	16 15 19.4	-32 55 05.0
		VV CrA	3.4	3.4	0.2	(unresolved)	19 03 06.8	-37 12 49.3
		S CrA	3.7	5.4	0.2	3.12 ± 0.81	19 01 08.6	-36 57 20.3
		DG CrA		< 0.6[c]	0.2	–	19 01 54.4	-37 23 40.5
20080805	6.65	MY Lup	1.3	2.9	0.1	4.75 ± 1.31	16 00 44.6	-41 55 31.5
		IM Lup	2.2	2.2	0.2	(unresolved)	15 56 09.2	-37 56 06.0

[a] Continuum flux and position are from fits in the (u, v) plane. For sources that were detected at 3σ, both the point-source flux (P) and the integrated flux for a Gaussian (G) are shown. For sources that were not detected, the coordinates of the phase centre are quoted.

[b] Calculated from the cleaned image.

[c] Quoted value is 3σ upper limit.

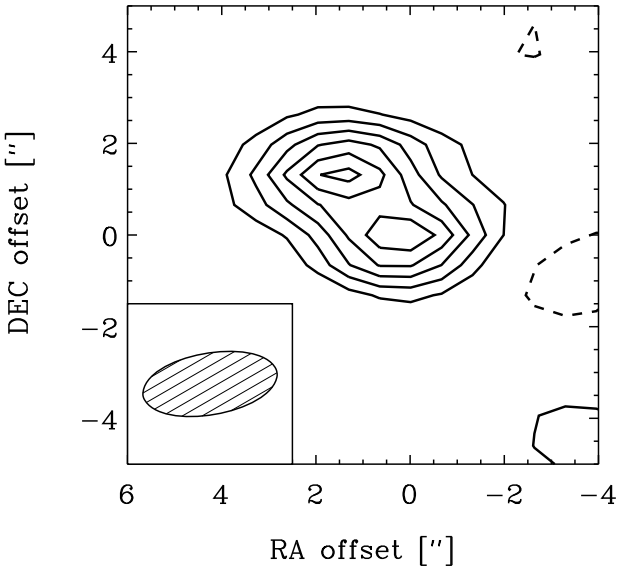

Figure 4.10: Image of VV CrA, observed at 3.2 mm on 2 and 3 August 2008. The offsets are with respect to the phase centre, which is located at 19:03:06.7, -37:12:49.7. The contours are at 2, 4, 6, ... times the rms of 2.0 mJy/beam; negative contours are dashed.

were obtained in both occasions, they were co-added in the (u, v) plane to improve the signal-to-noise ratio. The resulting fluxes or 3σ upper limits are presented in Tables 4.4 and 4.5. The amplitude as a function of (u, v) distance of the sources detected with CARMA at 1 mm is plotted in Fig. 4.13, that of the sources detected with CARMA at 3 mm in Fig. 4.14.

The complete results of the VLA observations at 7 mm and 1 cm are shown in Table 4.17, those of the VLA observations at 3.5 and 6.2 cm in Table 4.18.

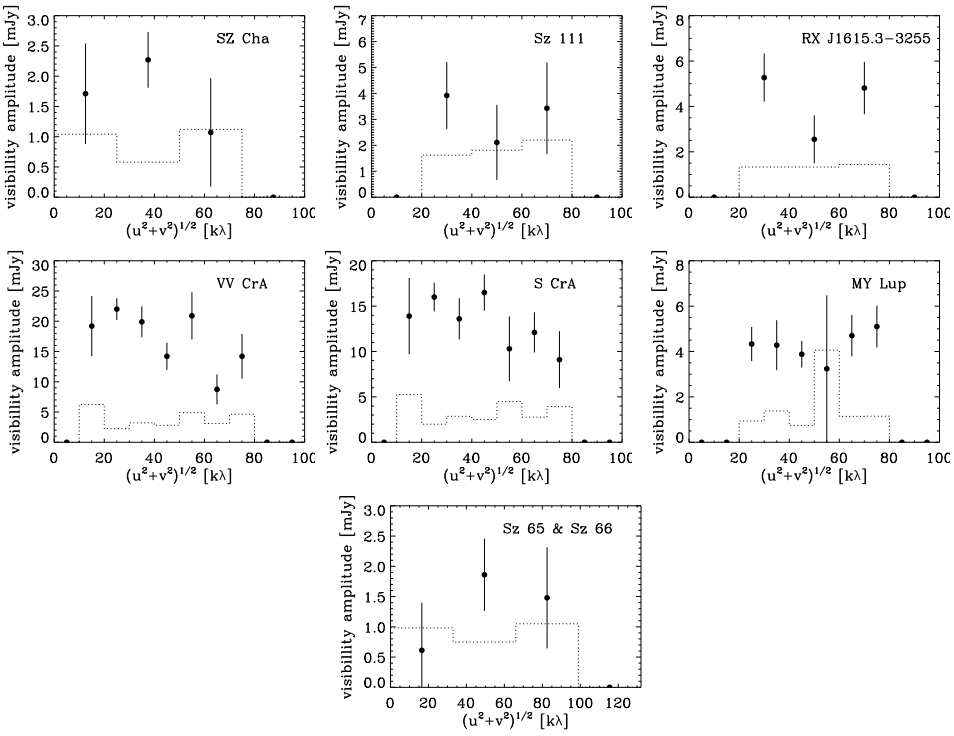

Figure 4.11: Amplitude as a function of (u, v) distance for sources detected with the ATCA at 3 mm. The data points give the vector-averaged amplitude per bin, where the data are binned in annuli according to (u, v) distance. The error bars show the statistical 1σ errors and the dotted lines give the expected amplitude for zero signal.

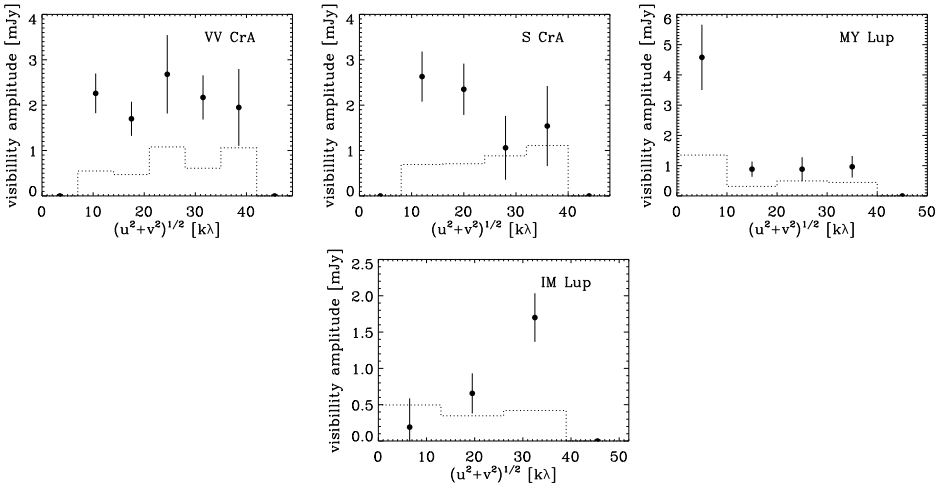

Figure 4.12: Amplitude as a function of (u, v) distance for sources detected with the ATCA at 7 mm. The data points give the vector-averaged amplitude per bin, where the data are binned in annuli according to (u, v) distance. The error bars show the statistical 1σ errors and the dotted lines give the expected amplitude for zero signal.

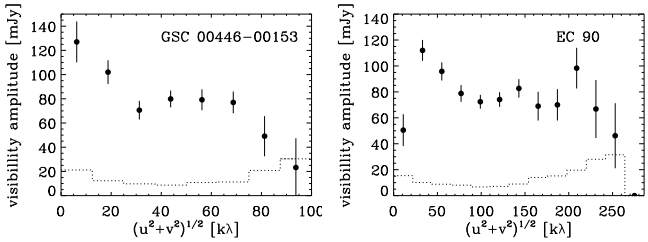

Figure 4.13: Amplitude as a function of (u, v) distance for sources detected with CARMA at 1 mm. The data points give the vector-averaged amplitude per bin, where the data are binned in annuli according to (u, v) distance. The error bars show the statistical 1σ errors and the dotted lines give the expected amplitude for zero signal.

Table 4.15: Complete results of CARMA observations at 1 mm.

Obs. date	$\lambda_{\rm eff}$ (mm)	Target source[a]	Continuum flux[b] (P)	(G)	rms[c]	Gaussian size (arcsec)	RA[b] (J2000)	Dec[b] (J2000)
20080518	1.33	GSC 00446-00153	43.6	50.5	6.0	0.46 ± 0.32	18 30 06.2	+00 42 33.6
20080620	1.33	EC 82	< 15.7[d]		5.2	–	18 29 56.8	+01 14 46.0
		EC 90	91.8	91.7	10.4	(unresolved)	18 29 57.7	+01 14 07.0
		18290088+0029315	< 16.4[d]		5.5	–	18 29 00.9	+00 29 31.6
		IRAS 18268-0025	< 15.6[d]		5.2	–	18 29 28.2	-00 22 57.1
		CoKu Ser G3	< 17.1[d]		5.7	–	18 29 01.8	+00 29 54.6
		VV Ser	< 14.8[d]		4.9	–	18 29 47.9	+00 08 40.0
		18285808+0017244	< 24.6[d]		8.2	–	18 28 58.1	+00 17 24.4
		18285020+0009497	< 98.2[d]		32.7	–	18 28 50.2	+00 09 49.7
20080704	1.33	EC 97	< 23.3[d]		7.8	–	18 29 58.2	+01 15 22.0
		18285020+0009497	< 22.8[d]		7.6	–	18 28 50.2	+00 09 49.7
		18294410+0033561	< 15.0[d]		5.0	–	18 29 44.1	+00 35 56.1
		18293619+0042167	< 8.7[d]		2.9	–	18 29 36.2	+00 42 16.7
		GSC 00446-00153	90.8	97.6	2.8	0.67 ± 0.23	18 30 06.2	+00 42 33.6

[a] In the case of SSTc2d names, only the coordinates (in J2000) are shown.

[b] Continuum flux and position are from fits in the (u, v) plane. For sources that were detected at 3σ, both the point-source flux (P) and the integrated flux for a Gaussian (G) are shown. For sources that were not detected, the coordinates of the phase centre are quoted.

[c] Calculated from the cleaned image.

[d] Quoted value is 3σ upper limit.

Table 4.16: Complete results of CARMA observations at 3 mm.

Obs. date	$\lambda_{\rm eff}$ (mm)	Target source[a]	Continuum flux[b] (P)	(G)	rms[c]	Gaussian size (arcsec)	RA[b] (J2000)	Dec[b] (J2000)
20080618	3.15	EC 82		< 2.9[d]	1.0	–	18 29 56.8	+01 14 46.0
		EC 90	11.3	11.6	1.0	1.69 ± 0.97	18 29 57.8	+01 14 06.9
		18290088+0029315	3.4	3.9	0.6	(unresolved)	18 29 00.9	+00 29 31.7
		IRAS 18268-0025		< 1.9[d]	0.6	–	18 29 28.2	-00 22 57.1
		CoKu Ser G3		< 1.6[d]	0.5	–	18 29 01.8	+00 29 54.6
		VV Ser		< 1.8[d]	0.6	–	18 28 47.9	+00 08 40.0
20080619	3.15	18285808+0017244		< 1.9[d]	0.6	–	18 28 58.1	+00 17 24.4
		18285020+0009497		< 1.9[d]	0.6	–	18 28 50.2	+00 09 49.7
		18294410+0033561		< 1.7[d]	0.6	–	18 29 44.1	+00 33 56.1
		18293619+0042167		< 2.7[d]	0.9	–	18 29 36.2	+00 42 16.7
20080622	3.15	18293619+0042167		< 5.3[d]	1.8	–	18 29 36.2	+00 42 16.7
		GSC 00446-00153	6.8	8.1	1.0	2.71 ± 1.58	18 30 06.3	+00 42 34.2

[a] In the case of SSTc2d names, only the coordinates (in J2000) are shown.

[b] Continuum flux and position are from fits in the (u, v) plane. For sources that were detected at 3σ, both the point-source flux (P) and the integrated flux for a Gaussian (G) are shown. For sources that were not detected, the coordinates of the phase centre are quoted.

[c] Calculated from the cleaned image.

[d] Quoted value is 3σ upper limit.

Table 4.17: Complete results of VLA observations at 6.9 mm and 1.3 cm.

Obs. date	$\lambda_{\rm eff}$ (mm)	Target source[a]	Continuum flux[b] (Peak)	(Integ.)	rms[c]	Gaussian size (arcsec)	RA[b] (J2000)	Dec[b] (J2000)
20080310	6.93	CoKu Ser G3	$< 1.2^{\rm d}$		0.4	–	18 29 01.8	+00 29 54.5
		18290088+0029315	$< 0.7^{\rm d}$		0.2	–	18 29 00.9	+00 29 31.5
		EC 90	$< 1.0^{\rm d}$		0.3	–	18 29 57.7	+01 14 05.7
		VV Ser	$< 0.7^{\rm d}$		0.2	–	18 28 47.9	+00 08 39.8
		EC 97	$< 0.6^{\rm d}$		0.2	–	18 29 58.2	+01 15 21.7
		18285020+0009497	$< 0.6^{\rm d}$		0.2	–	18 28 50.2	+00 09 49.6
		EC 82	$< 0.5^{\rm d}$		0.2	–	18 29 56.9	+01 14 46.4
20080311	13.4	CoKu Ser G3	8.66	9.81	0.06	1.17×0.91	18 29 01.8	+00 29 54.8
		18290088+0029315	$< 0.17^{\rm d}$		0.06	–	18 29 00.9	+00 29 31.5
		EC 90	$< 0.24^{\rm d}$		0.08	–	18 29 57.7	+01 14 05.7
		VV Ser	$< 0.17^{\rm d}$		0.06	–	18 28 47.9	+00 08 39.8
		EC 97	$< 0.15^{\rm d}$		0.05	–	18 29 58.2	+01 15 21.7
20080313	13.4	18285020+0009497	$< 0.20^{\rm d}$		0.07	–	18 28 50.2	+00 09 49.6
		18290980+0034459	$< 0.23^{\rm d}$		0.08	–	18 29 09.8	+00 34 45.8
		EC 82	$< 0.28^{\rm d}$		0.09	–	18 29 56.9	+01 14 46.4

[a] In the case of SSTc2d names, only the coordinates (in J2000) are shown.

[b] Continuum flux and position are obtained using the AIPS task JMFIT, which fits elliptical Gaussians to the cleaned image. For sources that were detected at 3σ, both the peak (Peak) and the integrated (Integ.) flux are shown. For sources that were not detected, the coordinates of the phase centre are quoted.

[c] Calculated from the cleaned image.

[d] Quoted value is 3σ upper limit.

Table 4.18: Complete results of VLA observations at 3.5 and 6.2 cm.

Obs. date	$\lambda_{\rm eff}$ (mm)	Target source[a]	Continuum flux[b] (Peak)	(Integ.)	rms[c]	Gaussian size (arcsec)	RA[b] (J2000)	Dec[b] (J2000)
20080314	35.5	EC 82	< 0.09[d]		0.03	–	18 29 56.0	+01 14 49.9
		EC 90	< 0.09[d]		0.03	–	18 29 56.0	+01 14 49.0
		EC 97	< 0.09[d]		0.03	–	18 29 56.0	+01 14 49.0
		CoKu Ser G3	1.11	1.11	0.03	2.49×2.35	18 29 01.8	+00 29 54.7
		18290088+0029315	< 0.10[d]		0.03	–	18 29 05.0	+00 29 44.0
		VV Ser	0.14	0.17	0.03	3.25×2.31	18 28 47.9	+00 08 40.1
		18285020+0009497	< 0.08[d]		0.03	–	18 28 40.0	+00 09 13.0
20080315	61.7	EC 82	< 0.09[d]		0.03	–	18 29 57.0	+01 14 40.0
		EC 90	< 0.09[d]		0.03	–	18 29 57.0	+01 14 40.0
		EC 97	< 0.09[d]		0.03	–	18 29 57.0	+01 14 40.0
		CoKu Ser G3	0.91	1.00	0.04	(unresolved)	18 29 01.9	+00 29 54.9
		18290088+0029315	< 0.12[d]		0.04	–	18 29 07.0	+00 32 09.0
		VV Ser	< 0.14[d]		0.05	–	18 29 47.0	+00 09 11.0
		18285020+0009497	< 0.14[d]		0.05	–	18 29 47.0	+00 09 11.0

[a] In the case of SSTc2d names, only the coordinates (in J2000) are shown.

[b] Continuum flux and position are obtained using the AIPS task JMFIT, which fits elliptical Gaussians to the cleaned image. For sources that were detected at 3σ, both the peak (Peak) and the integrated (Integ.) flux are shown. For sources that were not detected, the coordinates of the phase centre are quoted.

[c] Calculated from the cleaned image.

[d] Quoted value is 3σ upper limit.

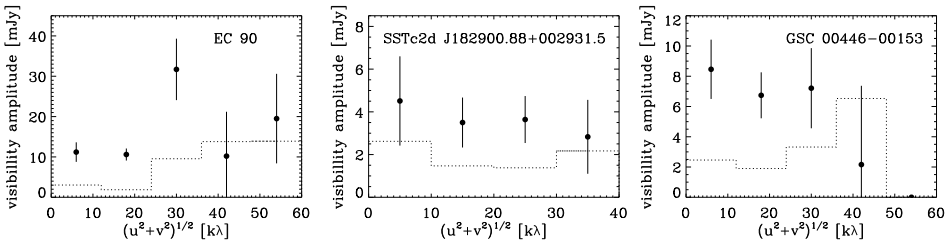

Figure 4.14: Amplitude as a function of (u, v) distance for sources detected with CARMA at 3 mm. The data points give the vector-averaged amplitude per bin, where the data are binned in annuli according to (u, v) distance. The error bars show the statistical 1σ errors and the dotted lines give the expected amplitude for zero signal.